

Dynamics of L–H transition and I-phase in EAST

This content has been downloaded from IOPscience. Please scroll down to see the full text.

View [the table of contents for this issue](#), or go to the [journal homepage](#) for more

Download details:

IP Address: 132.239.66.163

This content was downloaded on 14/01/2015 at 16:27

Please note that [terms and conditions apply](#).

Dynamics of L–H transition and I-phase in EAST

G.S. Xu^{1,9}, H.Q. Wang^{1,9}, M. Xu², B.N. Wan¹, H.Y. Guo¹, P.H. Diamond^{3,4}, G.R. Tynan³, R. Chen¹, N. Yan^{1,6}, D.F. Kong¹, H.L. Zhao¹, A.D. Liu⁵, T. Lan⁵, V. Naulin⁶, A.H. Nielsen⁶, J. Juul Rasmussen⁶, K. Miki⁷, P. Manz⁸, W. Zhang¹, L. Wang¹, L.M. Shao¹, S.C. Liu¹, L. Chen¹, S.Y. Ding¹, N. Zhao¹, Y.L. Li¹, Y.L. Liu¹, G.H. Hu¹, X.Q. Wu¹ and X.Z. Gong¹

¹ Institute of Plasma Physics, Chinese Academy of Sciences, Hefei 230031, People's Republic of China

² Southwestern Institute of Physics, PO Box 432, Chengdu 610041, People's Republic of China

³ CMTFO, University of California, San Diego, 9500 Gilman Drive, La Jolla, CA 92093, USA

⁴ WCI Center for Fusion Theory, National Fusion Research Institute, Daejeon 305–333, Korea

⁵ CAS Key Laboratory of Geospace Environment, Department of Modern Physics, University of Science and Technology of China, Hefei 230026, People's Republic of China

⁶ Association EURATOM-DTU, Department of Physics, Technical University of Denmark, DK 2800 Kgs. Lyngby, Denmark

⁷ Center for Computational Science and e-Systems, Japan Atomic Energy Agency, Kashiwa, Chiba 277–8587, Japan

⁸ Max-Planck-Institut für Plasmaphysik, EURATOM Assoziation, Boltzmannstr. 2, 85748 Garching, Germany

E-mail: gsxu@ipp.ac.cn and hqwang@ipp.ac.cn

Received 27 February 2014, revised 22 June 2014

Accepted for publication 5 August 2014

Published 16 September 2014

Abstract

The turbulence and flows at the plasma edge during the L–I–H, L–I–L and single-step L–H transitions have been measured directly using two reciprocating Langmuir probe systems at the outer midplane with several newly designed probe arrays in the EAST superconducting tokamak. The $E \times B$ velocity, turbulence level and turbulent Reynolds stress at ~ 1 cm inside the separatrix ramp-up in the last ~ 20 ms preceding the single-step L–H transition, but remain nearly constant near the separatrix, indicating an increase in the radial gradients at the plasma edge. The kinetic energy transfer rate from the edge turbulence to the $E \times B$ flows is significantly enhanced only in the last ~ 10 ms and peaks just prior to the L–H transition. The $E \times B$ velocity measured inside the separatrix, which is typically in the electron diamagnetic drift direction in the L-mode, decays towards the ion diamagnetic drift direction in response to fluctuation suppression at the onset of the single-step L–H, L–I–L as well as L–I–H transitions. One important distinction between the L–I–H and the L–I–L transitions has been observed, with respect to the evolution of the edge pressure gradient and mean $E \times B$ flow during the I-phase. Both of them ramp up gradually during the L–I–H transition, but change little during the L–I–L transition, which may indicate that a gradual buildup of the edge pedestal and mean $E \times B$ flow during the I-phase leads to the final transition into the H-mode. In addition, the transition data in EAST strongly suggest that the divertor pumping capability is an important ingredient in determining the transition behaviour and power threshold.


Keywords: L–H transition, I-phase, reciprocating probe, zonal flows, Reynolds stress

(Some figures may appear in colour only in the online journal)

1. Introduction

The L–H transition dynamics near the power threshold have attracted significant attention recently, stimulated by the ITER requirement for H-mode operation in the initial phase with

only limited power available [1]. The total auxiliary heating power at the beginning of ITER operation is ~ 73 MW, which is only slightly above the predicted threshold power for the H-mode access in ITER, i.e., ~ 52 MW, in a deuterium plasma at half of the nominal ITER H-mode density [2]. In hydrogen or helium plasmas, the required threshold power could be even higher [3]. To minimize the uncertainty in the threshold power prediction for ITER, a deeper physics-based understanding of the microscopic dynamics behind the macroscopic power threshold is required.

 Content from this work may be used under the terms of the [Creative Commons Attribution 3.0 licence](https://creativecommons.org/licenses/by/3.0/). Any further distribution of this work must maintain attribution to the author(s) and the title of the work, journal citation and DOI.

⁹ Authors to whom any correspondence should be addressed.

When the input heating power is near the L–H transition threshold power or as it passes through the threshold with a slow ramping rate, an intermediate oscillatory phase between the L and H phases, so-called ‘I-phase’, may appear prior to the final transition into the H-mode, with ‘dithering cycles’, i.e., a periodic oscillation between high and low confinement at the plasma edge, a phenomenon first noticed in DIII-D [4]. The associated L–H transition is termed ‘L–I–H transition’. It is characterized by a coherent oscillation in the $D\alpha/H\alpha$ emissions due to repetitive reduction of turbulence fluctuations and cross-field transport at the plasma edge. The terms ‘intermediate phase’ and ‘mesophase’ were first used in reference [5], where a model was proposed by Itoh, predicting ‘limit cycle oscillations’ (LCOs) near the L–H transition boundary. However, there was no clear distinction between the LCOs and the type III ELMs at that time. Experimentally, the type III ELMs, which also occur near the power threshold, can be distinguished from the LCOs by the occurrence of precursor oscillations. This distinction was first noticed in ASDEX [6], where the I-phase was termed as ‘dithering H-mode’ and the associated L–H transition was referred to as ‘dithering transition’. From terminological point of view, strictly speaking, the two terms, i.e., ‘I-phase’ and ‘dithering transition’, are not equivalent. The former refers in particular to a coherent oscillatory phenomenon, which is identified with a well-defined (perhaps evolving) frequency. The latter is a more general term, which makes no distinction between the coherent oscillations and the chaotic, repeating (incoherent) back-and-forth L–H and H–L transitions. The appearance of the I-phase strongly depends on the diverter configuration. The I-phase was further studied in ASDEX Upgrade [7–10] and JET [11]. An extension of Itoh’s LCO model was used to explain the dynamic behaviour [7]. The temporal behaviour at the plasma edge during the I-phase was measured with the high-resolution ECE in ASDEX Upgrade [9] and heavy ion beam probe (HIBP) in JFT-2M [12], indicating the periodic buildup and collapse of a weaker edge transport barrier in comparison with that in the H-mode. The I-phase was also observed in W7-AS stellarator [13, 14], H-1 Helic [15], and recently in TJ-II stellarator [16–18], suggesting that it is not a unique phenomenon for tokamaks.

Beam emission spectroscopy (BES) measurements in DIII-D during the L–I–H transition showed that the temporal evolution of edge fluctuation levels appears to lead the poloidal phase velocity, suggesting a predator–prey-type relationship between the edge turbulence and the self-generated shear flows [19, 20]. Stimulated by the DIII-D’s results, a predator–prey model for the L–I–H transition was proposed by Kim and Diamond [21], where the oscillatory behaviour at the transition is thought to be induced by a predator–prey interaction between the edge turbulence and the turbulence-driven zonal flows (ZFs). The final transition into the H-mode is secured by the ion-pressure-gradient-driven mean $E \times B$ flows (MFs), i.e., the so-called ‘diamagnetic flows’ (the diamagnetic component of the $E \times B$ flow, $\nabla p_i / (Z_i e n_i B)$). Note that, here ‘securing the transition’ means maintaining the H-mode state and preventing back transition, which is different from ‘triggering the transition’. Recently, this model was extended from 0D (zero-dimensional) to 1D in space [22, 23], showing that the LCO appears as a nonlinear wave originating from the

separatrix, propagating inwards. It also succeeds in predicting the I-phase and hysteresis at the H–L back transition [24] and the stimulated L–H transition by the supersonic molecular beam injection (SMBI) [25, 26].

Significant progress has been made over the last three years in understanding the transition dynamics, partially due to remarkable improvement in temporal resolution for turbulence and flow measurements at the plasma edge. Experiments mainly focused on the I-phase, which allows study of the transition dynamics on an expanded timescale. These efforts started from the experiments in NSTX [27] and TJ-II [16], using gas puff imaging (GPI) and reflectometer, respectively, followed by the experiments in ASDEX Upgrade using Doppler reflectometer, indicating that the LCO arises from the competition between the edge turbulence and the geodesic acoustic modes (GAMs) [28]. However, the GAMs were observed to decrease in amplitude or to be absent in several machines, as approaching the transition threshold conditions, e.g., DIII-D [29, 30] and HL-2A [31]. Evidence for the low-frequency ZFs playing a role in the LCO dynamics was obtained in EAST using toroidally separated two reciprocating probes [32]. It was found that periodic turbulence suppression occurs when the radial electric field (E_r) shearing rate transiently exceeds the turbulence decorrelation rate at the plasma edge. The spatiotemporal structure of the LCO was further studied in TJ-II [17, 18] and DIII-D [33] using Doppler reflectometer, in NSTX [34] and C-Mod [35] using GPI. Evidence for triggering the L–H transition by ZFs with a sufficient strong Reynolds stress was obtained in EAST using a triple-probe array [36]. Furthermore, the LCO was also observed in the H-mode ELM-free phase at marginal input power in EAST, exhibiting a modulation interaction between the $E \times B$ flows and a high-frequency turbulence (in contrast to the low-frequency turbulence in the L-mode) in the steep-gradient pedestal region [37, 38]. In addition, the turbulence Reynolds work, i.e., the kinetic energy transfer rate from the edge turbulence to the sheared flows, has been measured directly during the I-phase with probe arrays in DIII-D [39] and with a newly developed dual GPI system in EAST [40], showing significant magnitude at the plasma edge. This provides a strong support of the predator–prey model for the ZF-driven LCO [21].

More recently, probe measurements in HL-2A [41] showed a new type of LCO (so-called type-J) in addition to the ZF-driven LCO (so-called type-Y), which was claimed to challenge the predator–prey model [21]. In the type-J LCO, the edge $E \times B$ flow leads the turbulence intensity rather than lags behind it in the type-Y LCO. It seems to be contradictory to the assumption of turbulence-driven flows in terms of causality. The type-J LCO was also found in JFT-2M recently [42] with a careful reanalysis of HIBP data, and the Reynolds stress was found too small to account for the flow acceleration in the LCO. Furthermore, it was reconfirmed recently that the time sequences in the DIII-D experiments [33, 43] are actually consistent with the type-J rather than the type-Y LCO. It is currently thought that the type-J LCO may not be interpreted in terms of the ZFs. In contrast, the MFs are proposed to be the drive for the type-J LCO. However, open questions still exist on this. The MFs will principally introduce a positive feedback, which is unlikely to constitute a closed cycle without

involving other feedback loops. More recently, it was pointed out that turbulence and pressure gradient constitute another predator–prey pair in addition to the ZF–turbulence pair [44]. If this predator–prey pair dominates over the system, one will see the type-J LCO. A new model has been developed recently by introducing a predator–prey response delay time into the Kim–Diamond model, which successfully reproduces a smooth transition from the type-Y to the type-J LCO.

The characteristics of the LCOs in different machines are not the same. The LCOs observed in NSTX [27], C-Mod [35], JFT-2M [41] and the 2010 experiments in EAST [32] have relatively smaller amplitude and/or higher frequency relative to the normal LCOs such as those seen in DIII-D [33] and EAST [40], and typically appear preceding a clearly defined single-step H-mode transition. Both small-amplitude LCOs and the normal LCOs have been observed in EAST. To further investigate the dynamics of L–H transition and I-phase in EAST, detailed measurements have been made slightly inside the separatrix, and in the scrape-off layer (SOL) as well, using several newly designed multi-tipped probe arrays mounted on the two reciprocating probe systems in EAST, including the Mach probes and a diamond-coated triple-probe array, which allows measurements up to 1.5 cm inside the separatrix near the transition conditions. More information at the plasma edge has been provided simultaneously with these probes, including E_r , electron pressure gradient, turbulence-driven radial particle flux, parallel ion flow velocity, and radial gradient of turbulent Reynolds stress. Some interesting new observations have been obtained, which may have significant implications for the dynamics behind the L–H transition and I-phase.

It is difficult to provide radial multiple-point profile measurements with the Langmuir probe inside the separatrix near the transition conditions. However, it is still the unique diagnostic for some important physical quantities with high time resolution at the plasma edge. For instance, only probes or HIBP can provide the direct measurements of the E_r and $E \times B$ velocity. The flow velocity measured by Doppler reflectometer, GPI and BES is actually the propagation velocity of plasma fluctuations, which can be used as an estimation of the $E \times B$ velocity only when the fluctuation phase velocity in the plasma frame is much smaller than the $E \times B$ velocity [33].

The remainder of this paper is organized as follows: section 2 gives a brief introduction of the two reciprocating probe systems on EAST, which is the main diagnostic for this study. The experimental setup and a global description of the experiments are also presented. Section 3 presents the probe measurements of a single-step L–H transition. Section 4 presents the probe measurements of an L–I–L transition. Section 5 studies the L–I–H transition with a 3×4 -tip probe array slightly inside the separatrix. Section 6 shows the SOL behaviours during the L–I–H transition measured by a 12-tip probe array in the SOL and a four-tip probe array right at the separatrix. Section 7 shows the magnetic perturbations associated with the LCOs and comparisons are made with those associated with type III ELMs. Section 8 reports the small-amplitude LCOs [32], which is a special type of LCOs, appearing prior to the L–H transition or mixed with the normal LCOs. Triggering of the small-amplitude LCOs by sawteeth is also presented. Discussions and summary are given in section 9.

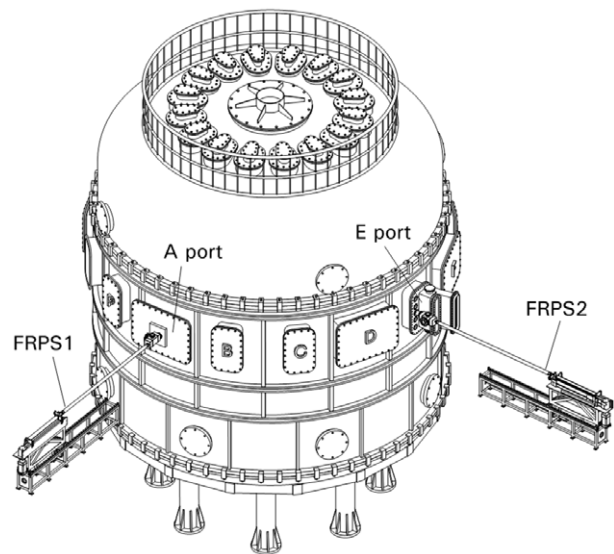


Figure 1. EAST tokamak and two reciprocating probe systems, toroidally separated by 89° .

2. Main diagnostics and experimental setup

The experiments were carried out on the EAST superconducting tokamak [45]. EAST is a medium-sized tokamak with modern divertor configurations and actively water-cooled plasma facing components (PFCs), with plasma major radius $R_0 \sim 1.88$ m on the magnetic axis, minor radius $a \sim 0.44$ m. EAST equips with two reciprocating probe systems, located at the outer midplane in two horizontal ports, A and E, respectively, toroidally separated by 89° [46], as shown in figure 1. The fast reciprocating motion is driven by an ac servo motor system capable of scanning a radial distance of 50 cm at a speed of 2 m s^{-1} . The probe tips are made of graphite with cylindrical shape, typical length of ~ 2 mm and diameter of ~ 2 mm. The probe data are digitized with 12-bit resolution at a sampling rate of 5 MHz, which is sufficiently high to resolve the edge turbulence fluctuations with spectral power mostly below 500 kHz [32].

The L–H transition experiments reported in this paper were conducted with three different kinds of divertor configurations, i.e., lower single null (LSN), double null (DN) and upper single null (USN). We define ‘normal B_t ’ as being in the clockwise direction viewing from the top with ion $B \times \nabla B$ drift towards lower divertor, while ‘reversed B_t ’ in the counter-clockwise direction with ion $B \times \nabla B$ drift towards upper divertor. The toroidal magnetic field, B_t , and the plasma current, I_p , in EAST are both normally operated in the ‘reversed’ direction. But there are few shots in the 2012 campaign where B_t was operated in the ‘normal’ direction. The I_p direction has never changed. The data presented in this paper are all obtained with ‘reversed B_t ’, for which the LSN configuration is unfavourable in terms of the ion $B \times \nabla B$ drift direction, i.e., away from the active X-point. Figure 2 shows the configurations and some parameters in three typical shots where the probe data are available, i.e., 36030 (with a single-step transition at 3.52 s as presented in section 3), 39283 (with an L–I–L transition near 5.31 s as presented in section 4) and 42160 (with an L–I–H transition near 3.994 s as presented in

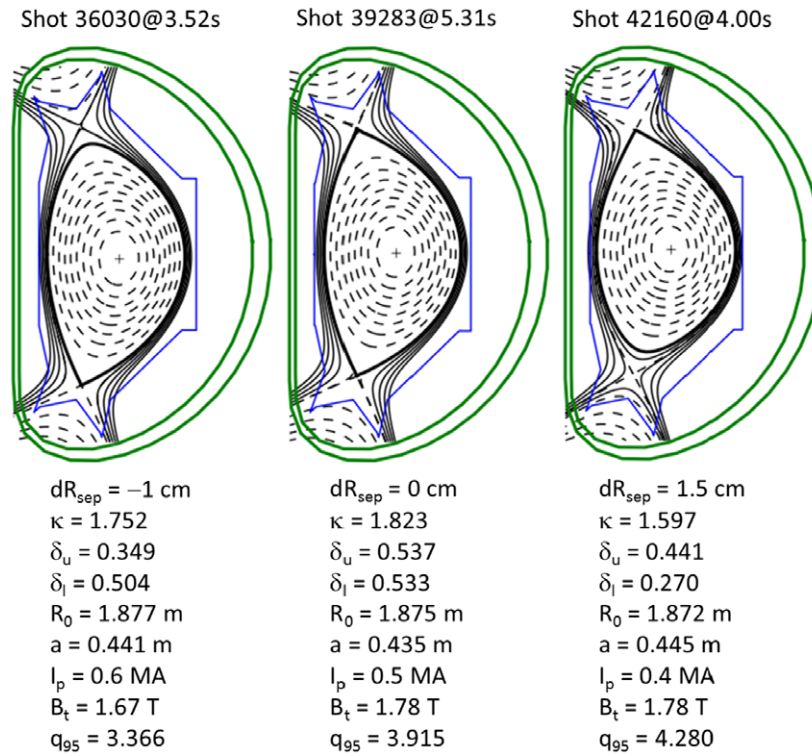


Figure 2. Plasma configurations and parameters in three typical shots where the probe data are available.

section 5). The distance between the primary and secondary separatrices at the outer midplane, dR_{sep} , are -1 cm, 0 cm and 1.5 cm, respectively. I_p was operated at 0.6 , 0.5 and 0.4 MA with B_t on the magnetic axis at 1.67 , 1.78 and 1.78 T. The edge safety factors, q_{95} , are 3.366 , 3.915 and 4.280 . The plasma elongation factor κ and the upper and lower triangularity, δ_u and δ_l , are also listed in figure 2.

The H-mode threshold power on EAST is near 1 MW with the central-line-averaged density, \bar{n}_e , at $1.7\text{--}3 \times 10^{19} \text{ m}^{-3}$ [47–50], which does not appear to depend on the detailed heating scheme [49], i.e., the H-mode can be achieved at the same absorption power level (~ 1 MW) with either lower hybrid current drive (LHCD) alone [47], ion cyclotron resonance frequency (ICRF) heating alone [48], or combined LHCD and ICRF heating schemes. To access the H-mode at this power level, extensive lithium (Li) wall coating with $10\text{--}30$ grams of Li through evaporation was applied daily (conducted before each-day's machine operation). The available source power for the LHCD at 2.45 GHz was 2 MW with $\sim 14\%$ transmission line loss and the launched parallel refractive index $n_{||}$ peaking at 2.1 . The ICRF was operated at ~ 27 MHz with on-axis power deposition via hydrogen minority resonance in the deuterium plasmas. To achieve the H-mode with the ICRF alone, 1.6 MW of injected power is required due to the relatively low absorption efficiency [48].

The appearance of the I-phase strongly depends on the diverter configuration. In the 2012 campaign, more than 1000 shots with the L–I–H transition have been obtained in total. Among them, $\sim 80\%$ are obtained in plasmas with DN configuration with the loss power through the plasma boundary varying in the range of $0.7\text{--}1.5$ times of the L–H transition threshold power, including several shots with ‘normal B_t ’.

The definition for the DN configuration is $|dR_{sep}| < 1$ cm. The core radiation power has been subtracted for the loss power calculation.

The LCO behaviour in the $D\alpha$ emission signals also varies significantly for different diverter configurations. The LCOs with DN configuration are mostly regular large-amplitude oscillations, typically exhibiting a clear and sharp transition from the L-mode to the I-phase, as shown in figure 9 (shot 39283), figure 15 (shot 40844), figure 19 (shot 38813) and figure 24 (shot 38618). The duration of I-phase with the favourable ion ∇B direction (normally USN with ‘reversed B_t ’) is usually very short in time, with only a few limit cycles, as shown in figure 13 (shot 42160), and the amplitude of limit cycles in the diverter $D\alpha$ emissions is smaller than those with DN configuration. The LCOs with the unfavourable ion ∇B direction (normally LSN with ‘reversed B_t ’) are more irregular in frequency and amplitude, and usually appear with increasing amplitude until the final transition into the ELM-free H-mode or decreasing amplitude at the H–L back transition, as shown in figure 18. Single-step L–H transitions are more easily obtained with LSN configuration. One example for such a single-step transition is shown in figure 3 (shot 36030). EAST only has one in-vessel cryopump which is located near the outer target of the lower divertor with a nominal pumping speed for deuterium of $\sim 75.6 \text{ m}^3 \text{ s}^{-1}$ [51]. The particle exhaust capability is therefore stronger with LSN configuration, which may explain the preference for the LSN configuration. The detailed statistical analysis of the L–I–H transitions and configuration dependence will be reported elsewhere. This paper focuses on the study of the transition dynamics based mainly on the reciprocating probe measurements.

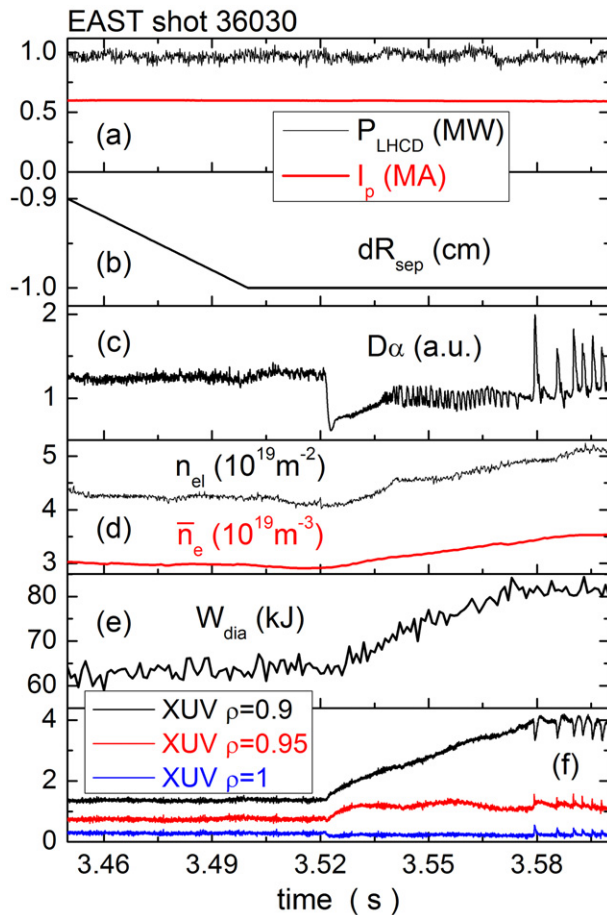


Figure 3. The time history of (a) LHCD input power and plasma current, (b) distance between the primary and secondary separatrix at the outer midplane, (c) divertor $D\alpha$ emission, (d) central-line-integrated density and central-line-averaged density, (e) plasma-stored energy from the diamagnetic measurement, (f) XUV radiations at the plasma edge, $\rho = 0.9$ black, 0.95 red and 1 blue.

3. Single-step L–H transition

With LSN configuration, the single-step L–H transition can be obtained with only 1 MW LHCD injected power plus ~ 0.3 MW ohmic power with \bar{n}_e at $3 \times 10^{19} \text{ m}^{-3}$, as shown in figure 3. The calculated loss power is very close to the L–H transition threshold power predicted by the international tokamak scaling [47]. The L–H transition occurs at about 20 ms after the configuration switched from DN to LSN with $dR_{\text{sep}} = -1$ cm. The L–H transition does not occur with DN configuration at the same power level and plasma density, which may imply that the threshold power is lower with LSN configuration (unfavourable ion ∇B direction with ‘reversed B_t ’). This is contrary to the observation in most other tokamaks, where the lowest power threshold is usually obtained with the favourable ion ∇B direction or DN configuration. This interesting observation has been reported in a recent publication [50].

The L–H transition is characterized by a single-step reduction in the divertor $D\alpha$ emission on the timescale of 1 ms, as shown in figure 3(c), then typically followed by a short ELM-free phase of several tens of ms with increasing plasma

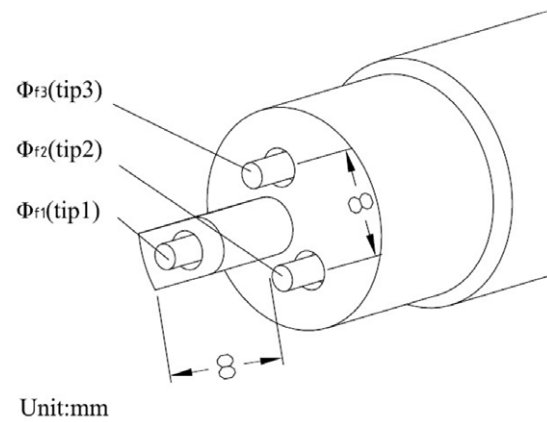


Figure 4. Layout of the diamond-coated three-tip probe array.

density (figure 3(d)) and stored energy (from the diamagnetic measurement) (figure 3(e)). Here, the central-line-integrated density is measured by a far infrared (FIR) laser interferometer with a laser line passing through the plasma centre. The pedestal formation is manifested by a continuous rise in the extreme ultra-violet (XUV) radiations at the plasma edge ($\rho = 0.95$ and 0.9) and a slight reduction near the separatrix ($\rho = 1$), as shown in figure 3(f). The XUV radiation mostly comes from the bremsstrahlung radiation with low impurity concentrations, which is proportional to $Z_{\text{eff}} n_e^2 T_e^{-1/2}$, where Z_{eff} is the effective charge number of the ions. Hence, the XUV radiation mainly reflects the density behaviour. The ELM-free phase finally transitions into the type III ELM phase at 3.58 s.

The L–H transition at 3.521 s shown in figure 3 was captured by the reciprocating Langmuir probes when the probe at port E reached to the radial position with the innermost tip at ~ 12 mm inside the separatrix (i.e., $\Delta r \equiv r - r_{\text{sep}} \sim -12$ mm) and stayed there for ~ 100 ms, while at the same time the probe in port A stayed in the SOL with the innermost tip near the separatrix (i.e., $\Delta r \sim 0$ mm). The probe radial position was confirmed by shot-by-shot position scan. The separatrix position is obtained from the EFIT reconstruction of the MHD equilibrium with an error bar of ~ 5 mm at the outer midplane.

To minimize the disturbance to the edge plasma and provide reliable measurements inside the separatrix as deeply as possible, two small probe heads with a diameter of 17 mm, a three-tip probe array and diamond-coated graphite probe shell have been used in this experiment, which are mounted on the two reciprocating probe systems, as shown in figure 4. Measurements of the L–H transition using big probe heads with a diameter larger than 30 mm deeply inside the separatrix are impracticable due to a serious disturbance to the edge plasma, which tends to prevent or delay the onset of the L–H transition. The diamond coating technique was developed recently by an institute in Austria [52]. It has been demonstrated to be very effective at reducing sputtering and impurity generation from the probe surface. In addition, the edge temperature is relatively low near the transition threshold conditions due to the low heating power in EAST, which allows for measurements much deeper into the plasma during the transitions with the diamond-coated graphite probes.

The three probe tips were used to measure floating potentials with two tips (Φ_{f2} and Φ_{f3}), poloidally separated

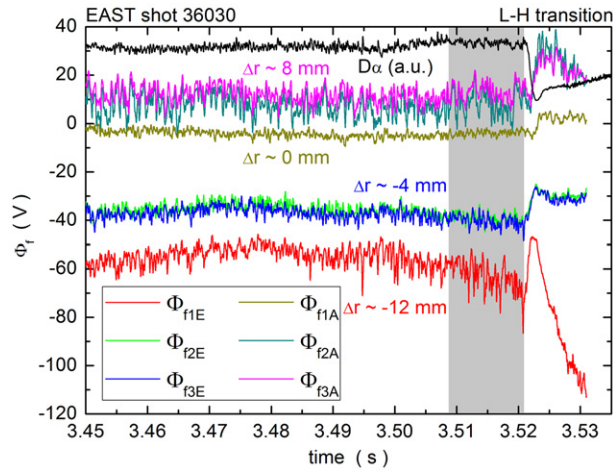


Figure 5. Floating potentials measured by two three-tip probe arrays, one at port E and the other at port A, and divertor $D\alpha$ emission.

by $d\rho = 8$ mm and a third tip (Φ_{f1}) in the middle of them, radially sticking out by $dr = 8$ mm. Such a probe array has been widely used in tokamak experiments to provide the direct measurements of E_r , electrostatic turbulent Reynolds stress, long-range correlation and ZF identification at the plasma edge [32, 36–39, 53–55]. The E_r is calculated as the radial gradient of the floating potential instead of the plasma potential, $E_r = [\Phi_{f1} - (\Phi_{f2} + \Phi_{f3})/2]/dr$, i.e., neglecting the contribution from the radial electron temperature (T_e) gradient. This may lead to overestimation of the negative E_r at the plasma edge [32, 36–39, 53–55]. The positive direction for E_r is defined as pointing outwards. The relationship between the plasma potential and floating potential is $\Phi_p = \Phi_f + \alpha T_e$, where α is a constant, which is taken as 2.5 throughout this paper. The coefficient α is predicted to be 2.8 in unmagnetized deuterium plasmas according to the standard probe sheath theory [56]. However, in a strongly magnetized plasma, α will be downshifted. There is currently no probe theory or empirical scaling in strongly magnetized plasmas to follow, so that there is still some uncertainty in the accuracy of the coefficient α . A more detailed discussion on this problem will be presented in section 9.

Figure 5 shows the six floating potential signals measured by the two three-tip probe arrays (one at port E and the other at port A) and the $D\alpha$ emission from the lower divertor region in the EAST (shot 36030). A first order low-pass digital Butterworth filter with the cutoff frequency at 2.5 kHz has been applied to the floating potential signals to remove high-frequency fluctuations. The zero-phase-shift forward and reverse digital infinite impulse response (IIR) filtering is used in the analysis throughout this paper to avoid introducing any phase shift during the filtering. The floating potentials appear to be positive in the SOL, i.e., Φ_{f2A} and Φ_{f3A} at $\Delta r \sim 8$ mm, slightly negative near the separatrix, i.e., Φ_{f1A} at $\Delta r \sim 0$ mm, and drop sharply to negative value inside the separatrix, i.e., Φ_{f1E} at $\Delta r \sim -12$ mm, Φ_{f2E} and Φ_{f3E} at $\Delta r \sim -4$ mm. They evolve very slowly before the L–H transition except in the last ~ 10 ms as highlighted by the grey shadow area in the figure. The floating potential measured by the innermost tip, i.e., Φ_{f1E} , appears to drop much faster towards the negative

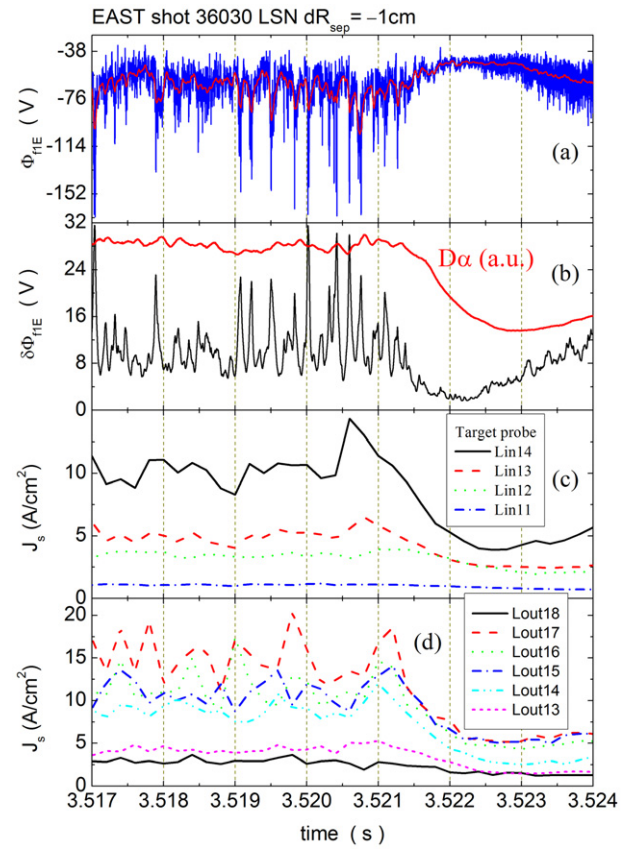


Figure 6. The time history of (a) floating potential measured by the innermost tip, i.e., Φ_{f1E} , and its filtered signal, (b) envelope of Φ_{f1E} fluctuation and divertor $D\alpha$ emission, (c) ion saturation current density measured by probe Lin11–14 on the inner target of the lower divertor and (d) measured by probe Lout13–18 on the outer target of the lower divertor.

direction in the last ~ 10 ms, while the floating potentials in the SOL remain nearly constant, indicating an increase in the radial gradient of floating potential at the plasma edge prior to the L–H transition.

Just before the L–H transition, a negative spike appears in Φ_{f1E} . Zooming in on the spike, one can see that the negative spike is actually composed of a series of intermittent negative spikes with a duration of $\tau \sim 10 \mu\text{s}$ for each spike, as shown in figure 6(a). Here, the original floating potential signal Φ_{f1E} (without filtering) is displayed, along with the signal after filtering. Figure 6(b) shows the envelope of Φ_{f1E} fluctuation and the divertor $D\alpha$ emission. The reduction in divertor $D\alpha$ emission appears to lag behind the fluctuation suppression at the outer midplane by hundreds of μs , which is largely consistent with the time required for SOL parallel transport along the magnetic field lines from the outer midplane to the divertor target plates. The fluctuation envelope appears to be very bursty and enhanced in amplitude just prior to the L–H transition. These negative spikes could be induced by a series of propagating plasma filaments as they pass the probe tips. The poloidal spatial size of the filaments can be evaluated as $\tau V_{\text{ph}} \sim 2$ cm, where the poloidal phase velocity, V_{ph} , is ~ -2.2 km s^{-1} in the electron diamagnetic drift direction at $\Delta r \sim -4$ mm, calculated from the cross correlation between Φ_{f2E} and Φ_{f3E} . In addition, according to $\Phi_f = \Phi_p - \alpha T_e$, the

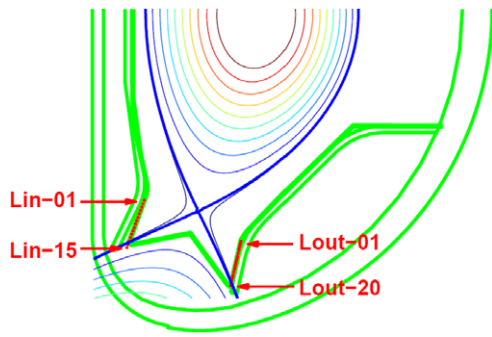


Figure 7. Distribution of the divertor Langmuir probes on the target plates.

appearance of negative spikes in the floating potential could be due to negative spikes in the plasma potential, Φ_p , or positive spikes in the electron temperature, T_e , i.e., the filaments are either negatively charged or hotter than the ambient plasma.

Fluctuation levels are significantly reduced at the L–H transition. At the same time, the floating potential at all radial locations change towards the positive direction, as shown in figure 5. The change in the SOL appears to lag behind that inside the separatrix by ~ 1 ms, on the same time scale for fluctuation suppression, indicating that the transition initiates at a radial location inside the separatrix. The change in the SOL appears to be a consequence of the fluctuation suppression and transport reduction across the separatrix. We notice that similar outward radial propagation of the transition front has been observed recently in the TJ-II stellarator [18]. In addition, similar positive change in the floating potential has been observed during the L–I–L transition, as shown in figure 10. The details will be presented in section 4. After the fluctuation suppression, Φ_{f1E} drops towards the negative direction, while the floating potentials in other channels do not change very much. This gives rise to an increasing radial gradient of the floating potential at the plasma edge. The Φ_{f1E} drop may be partially induced by edge T_e rise during the pedestal buildup following the L–H transition, recalling that $\Phi_f = \Phi_p - \alpha T_e$. Since there is no direct measurement of T_e in shot 36030, we cannot make a precise evaluation of the contribution from the T_e increase. However, with such low heating power, the edge T_e only modestly increases after the transition as shown in another shot in figure 13(j). Thus, the floating potential change may reflect an increase in the radial electric field as shown in figure 13(i).

Another interesting observation in this shot is from the divertor Langmuir probes. A bump in the divertor ion saturation current signals appears on the inner targets near the strike point just prior to the L–H transition, acting like a transition precursor. Figures 6(c) and (d) show the ion saturation current density measured by probe Lin11–14 on the inner target of the lower divertor and probe Lout13–18 on the outer target of the lower divertor. The locations of the probes relative to the strike points are shown in figure 7. The probe Lin14 and Lout17 are located near the inner and outer strike points, respectively, consistent with the EFIT reconstruction. Shot 36030 is a LSN discharge with $dR_{sep} = -1$ cm. A bump in Lin14 and Lin13 appear just prior to the L–H transition, and a weak bump can also be seen in Lin12. However, it is

unclear whether the bump also appears on the outer targets, since there are large-amplitude irregular fluctuations in the probe signals, as shown in figure 6(d). The bump may have been obscured by the fluctuations. The divertor probe data is digitized with a sampling rate of 5 kHz, which is much lower than the reciprocating probe data. The appearance of the bump seems to coincide with the enhanced fluctuation level just prior to the L–H transition, as measured by the midplane reciprocating probes. The bump has been observed in several shots before the L–H transitions, but not always.

The probe data in shot 36030 have been further analysed to look for a transition trigger mechanism through calculating the Reynolds work done by the turbulent Reynolds stress on the shear $\mathbf{E} \times \mathbf{B}$ flows, also known as the kinetic energy transfer from the turbulence into the shear flows or the shear flow production, $P_{\perp} \equiv \text{RS} (\partial V_E / \partial r)$ [36, 39, 40], where $V_E = E_r / B$ is the perpendicular $\mathbf{E} \times \mathbf{B}$ flow with the local magnetic field at the outer midplane, $B \sim 1.38$ T. The Reynolds stress is estimated as $\text{RS} \equiv \langle \delta v_r \delta v_p \rangle = \langle \delta E_p \delta E_r \rangle / B^2$, where $E_p = (\Phi_{f2} - \Phi_{f3}) / dp$, $dp = 8$ mm is the poloidal separation between tips 2 and 3, δ represents fluctuation components with frequency above 5 kHz where the turbulence dominates the spectrum, $\langle \dots \rangle$ denotes low-pass filtering using a second order low-pass digital Butterworth filter with the cutoff frequency at 0.5 kHz. The fluctuation components are extracted through high-pass filtering using a second order high-pass digital Butterworth filter with the cutoff frequency at 5 kHz. The results are shown in figure 8. The direct measurement of P_{\perp} development prior to the L–H transition or during the I-phase is considered as the key for demonstrating the essential role of the turbulence-driven ZFs in mediating the L–H transition, as suggested by the Kim–Diamond model [21], and also described in its updated version [22], where the model has been extended from 0D to 1D in space.

Regarding the Reynolds stress estimation, since the protruding tip is located exactly in the middle of the other two tips, there is no spatial offset between the measured poloidal electric field and the measured radial electric field, such that this three-tip probe array does not introduce any phase shift. This is a merit of such three-tip probe structure. Finite T_e fluctuations may introduce some uncertainty in the Reynolds stress estimation with the three-tip probe array. In principle, the electric field, either poloidal or radial, should be derived from the plasma potentials ($\Phi_p = \Phi_f + \alpha T_e$) rather than the floating potentials. However, the T_e fluctuation level is typically much smaller than the plasma potential fluctuation level at the plasma edge [46], therefore neglecting T_e fluctuation is valid in most cases.

Here, the $\mathbf{E} \times \mathbf{B}$ velocity shearing rate (radial gradient), $\partial V_E / \partial r$, is approximately evaluated as the radial difference between the two radial locations measured by the two probe arrays, i.e., $\Delta V_E / L_r$, where $L_r \sim 12$ mm. It clearly increases as the H-mode transition is approached in figure 8(b) up to ~ 153 kHz. The autocorrelation time of Φ_{f1E} floating potential fluctuations prior to the H-mode transition has also been measured, $\tau_{ac} \sim 6 \mu\text{s}$. Thus, the decorrelation rate of the turbulence is $\tau_{ac}^{-1} \sim 167$ kHz. The $\mathbf{E} \times \mathbf{B}$ velocity shearing rate appears to be comparable with the turbulence decorrelation rate just prior to the transition.

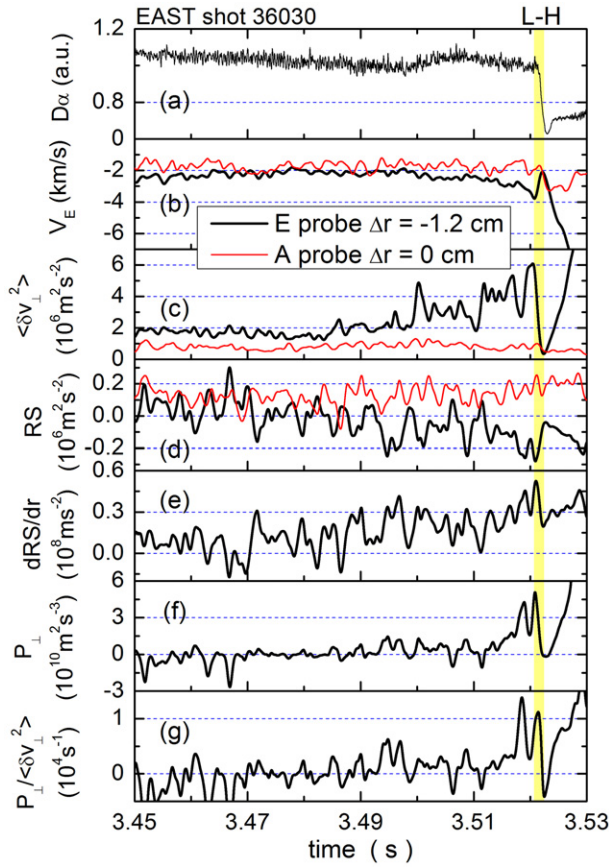


Figure 8. The time history of (a) divertor $D\alpha$ emission, (b) $E \times B$ velocities, black and red curves standing for that measured at port E and A, respectively, (c) mean-square fluctuation levels of the perpendicular $E \times B$ flows, (d) turbulent Reynolds stress, (e) the radial gradient of turbulent Reynolds stress, (f) shear flow production, (g) normalized shear flow production.

The $E \times B$ flows, V_E , measured by the probe array at port E appears to be enhanced in the electron diamagnetic drift direction (negative in the figure) from ~ -2 to ~ -4 km s $^{-1}$ before the L–H transition, however, without much change near the separatrix as measured by the probe array at port A, as shown in figure 8(b), suggesting an enhancement in the radial gradient of V_E prior to the transition. The increase starts from ~ 20 ms before the L–H transition when the divertor configuration is stabilized at LSN, and appears to accelerate in the last 10 ms.

At the same time, the fluctuation level is significantly enhanced inside the separatrix, however, keeps nearly constant near the separatrix, as shown in figure 8(c), where the mean-square fluctuation levels of the perpendicular $E \times B$ fluctuations, $\langle \delta v_{\perp}^2 \rangle = \langle \delta v_p^2 + \delta v_r^2 \rangle$, are displayed. Meanwhile, the turbulent Reynolds stress, RS, (figure 8(d)) and its radial gradient, dRS/dr , (figure 8(e)) ramps up with increasing fluctuation level. Here, the Reynolds stress gradient is measured by two radially displaced probe arrays, which are also toroidally displaced by a long distance, both located at the outboard midplane, so they are not on the same or neighbouring field lines, and the local turbulence measured at each location is uncorrelated. However, it is still valid to calculate the radial gradient like this, since implicitly, it is assumed that the derived

Reynolds stress is a flux-surface quantity. The same ensemble averaged Reynolds stress has been measured with the displaced probes simultaneously at the same radial location [37, 38], which justifies the assumption.

Note that the fluctuation level and the Reynolds stress appear to be temporarily reduced during the transition but then increase rapidly afterwards. It needs to be clarified that the fluctuations appearing after the transition are different from those before the transition, as shown in figure 6(a). Their frequency is much higher than the fluctuations before the transition. They have a rather broad frequency band (0.05–1 MHz), peaking at a frequency typically higher than 100 kHz [37, 38]. In contrast, the fluctuations before the transition are low-frequency fluctuations with most spectral power below 0.2 MHz. The low-frequency fluctuations are strongly suppressed during the transition and remain suppressed in the H-mode. Shortly after the transition, when the pedestal starts to build up, the high-frequency fluctuations appear in the steep-gradient pedestal region, leading to the recovery of the fluctuation level and the Reynolds stress. The high-frequency fluctuations are most frequently observed in the ELM-free H-mode phase following the transition and sometimes also observed in the inter-ELM phases with currently available heating power, which is up to two times of the transition threshold power. They are very likely induced by an unidentified microinstability other than that before the transition. The high-frequency fluctuations have been reported in detail in two recent papers [37, 38].

Figure 8(f) shows the calculated shear flow production, P_{\perp} , which appears to be significantly enhanced only in the last 10 ms and peaks just prior to the L–H transition. The normalized shear flow production, i.e., $P_{\perp}/\langle \delta v_{\perp}^2 \rangle$, provides a measure of the effective rate of kinetic energy transfer from the turbulence into the shear flows. It exceeds 1×10^4 s $^{-1}$ in the last few ms before the L–H transition. The rate is of the same order of the typical collisional damping rate of the poloidal flows, $\sim 1 \times 10^4$ s $^{-1}$, at the plasma edge [32, 37, 57]. In addition, we have estimated the time rate for the poloidal flow acceleration at the L–H transition, $\frac{1}{2} (1 + 2q_{95}^2) \partial_t (V_E^2)/\langle \delta v_{\perp}^2 \rangle \sim 1 \times 10^4$ s $^{-1}$, where the poloidal flow inertia is enhanced by a factor, $(1 + 2q_{95}^2) \sim 30$ [40], due to the well-known toroidal effect [5]. The collisionality at the plasma edge is in the plateau regime. The energy transfer rate from the turbulence to the poloidal flows is comparable with the time rate for the poloidal flow acceleration and also the time rate for the poloidal flow collisional damping, suggesting that the turbulence driving force is strong enough to account for the observed flow acceleration prior to the L–H transition. These results appear to be consistent with the picture that the turbulence-driven ZFs may play a role in mediating the L–H transition. Similar process of turbulence driving flows at the L–H transition has been recently observed in the DIII-D tokamak [58].

4. L–I–L transition

When the input heating power is very close to the L–H transition threshold power, the L–I–L transition is typically observed, i.e., a transition from L-mode via an I-phase, then back to L-mode. The L–I–H transitions are sometimes also observed when the power is considerably above, but still within

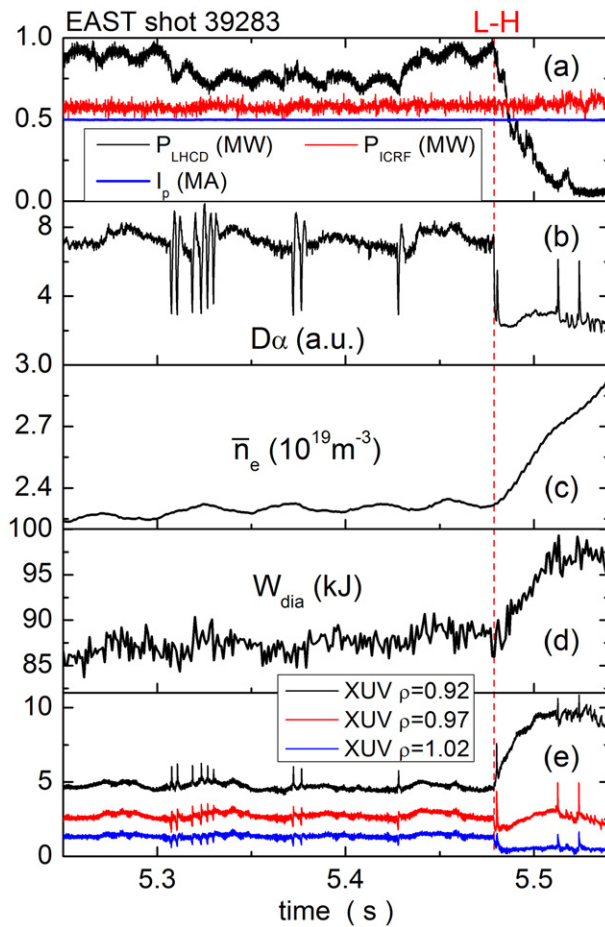


Figure 9. The time history of (a) LHCD, ICRF input power and plasma current, (b) divertor $D\alpha$ emission, (c) central-line-averaged density, (d) plasma-stored energy from the diamagnetic measurement, (e) XUV radiations at the plasma edge, $\rho = 0.92$ black, 0.97 red and 1.02 blue.

a factor of 1.5 of the threshold in EAST. However, the L–I–L transitions are only seen when the power was very marginal to the threshold. Furthermore, the duty cycle of the LCOs during the I-phase is different between the L–I–L transition and the L–I–H transition. The duty cycle is defined as the period for the transient enhancement of the edge fluctuations, τ_L , divided by the period for the transient suppression (i.e., quiescent period) of the edge fluctuations, τ_H . For a sin wave, the duty cycle, $\tau_L/\tau_H = 1$. It is observed in EAST that statistically the LCOs in the L–I–L transition have higher duty cycle than those in the L–I–H transition. For the L–I–L transition, the duty cycle is typically ≥ 1 , however, for the L–I–H transition, the duty cycle is typically ≤ 1 and usually progressively decreases as approaching the H-mode due to the extension of the quiescent periods as shown in figure 15.

Figure 9 shows a typical example for the L–I–L transition at marginal power, which is obtained in plasma with DN configuration as shown in figure 2. The I-phases appear intermittently with a few limit cycles, characterized by a series of dips in the divertor $D\alpha$ emissions due to suppression of the edge turbulence. The increase of the LHCD power leads to the final transition into the H-mode at 5.48 s with a single limit cycle at the transition. The two spikes in the H-mode are type III ELMs. The reduction of LHCD power after the

L–H transition is due to the degradation of the wave coupling with reduced plasma density in front of the launcher. The central-line-averaged density and the plasma-stored energy (from the diamagnetic measurement) do not change very much across the L–I–L transitions, in contrast to those after the L–H transition. The plasma-stored energy and XUV radiations at the plasma edge ramp-up during the ELM-free phase after the L–H transition until the appearance of the type III ELMs. Positive spikes are observed in the XUV radiation signal at the radial location of the H-mode pedestal top, i.e., $\rho = 0.92$, associated with the transient suppression period of the I-phase, negative spikes are observed at the pedestal foot, i.e., $\rho = 1.02$, and both positive and negative spikes are observed coexist in the edge steep-gradient region, i.e., $\rho = 0.97$, as shown in figure 9(e). This behaviour is different from that associated with the ELMs. For the ELMs, usually negative spikes appear at the pedestal top and positive spikes appear at the pedestal foot, behaving like sawteeth, as a natural result of the pedestal collapse, as shown in figures 3(f) and 9(e). Recalling that the XUV radiation signals mainly reflect the density behaviour, the spikes in the XUV signals may therefore suggest the periodic buildup of a weak density pedestal at the plasma edge during the quiescent period of the LCOs.

The first two limit cycles near 5.31 s were captured by the reciprocating Langmuir probe when the probe stayed at a radial position with the innermost tip at ~ 6 mm inside the separatrix ($\Delta r \sim -6$ mm) and another tip at $\Delta r \sim -3$ mm, i.e., the two tips are separated radially by $dr = 3$ mm, measuring the floating potential Φ_{f1} and Φ_{f2} , respectively. Their low-frequency components with the cutoff frequency at 2 kHz are shown in figure 10(b). The $E \times B$ flow velocity, $V_E = E_r/B$, is shown in figure 10(c), where the radial electric field is calculated as $E_r = (\Phi_{f1} - \Phi_{f2})/dr$, neglecting the contribution from the radial T_e gradient. Figure 10(d) shows the fluctuation envelopes, $|\delta\Phi_f + i * \text{Hilbert}(\delta\Phi_f)|$, where the Hilbert transform is used to compute the analytic signal. $\delta\Phi_f$ is the fluctuation components (> 10 kHz) of the floating potential, which is extracted through zero-phase-shift forward and reverse digital IIR filtering, using a second order high-pass digital Butterworth filter with the cutoff frequency at 10 kHz.

The fluctuation envelopes are significantly reduced at the L–I transition. The absolute fluctuation level measured by the inner tip is higher than the outer tip in the L-mode, and the reduction is more significant at the transition. We do not see significant change in either the fluctuation levels or the floating potentials prior to the fluctuation suppression. Hence, we do not know what triggers the fluctuation suppression at this point, based on the available probe data in figure 10. One speculation is that the fluctuation levels and floating potentials may change at deeper radial locations, like those shown in figure 5, however, here the probes are not deep enough into the edge plasma, such that they did not detect the change.

The floating potentials change towards the positive direction at the L–I transition. Similar change also occurs at the single-step L–H transition, as shown in figure 5. The calculated V_E (in the electron diamagnetic drift direction) is reduced at the plasma edge. The change occurs nearly at the same time of the fluctuation suppression, typically accomplished within 1 ms.

To examine the causality between the fluctuation suppression and the V_E change, the trajectory of the system in the

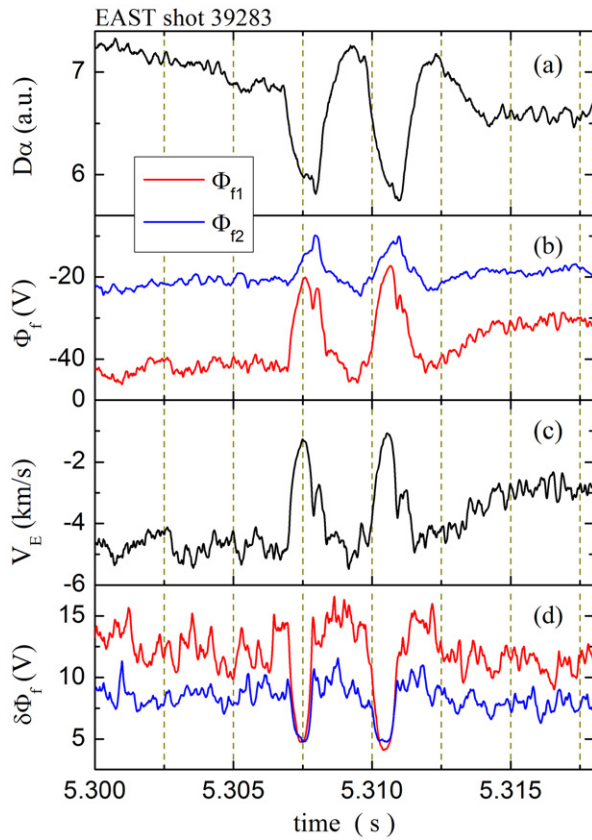


Figure 10. The time history of (a) divertor $D\alpha$ emission, (b) floating potentials, Φ_{f1} at $\Delta r \sim -6$ mm and Φ_{f2} at $\Delta r \sim -3$ mm, (c) $E \times B$ flow velocity, (d) fluctuation envelopes of the floating potentials.

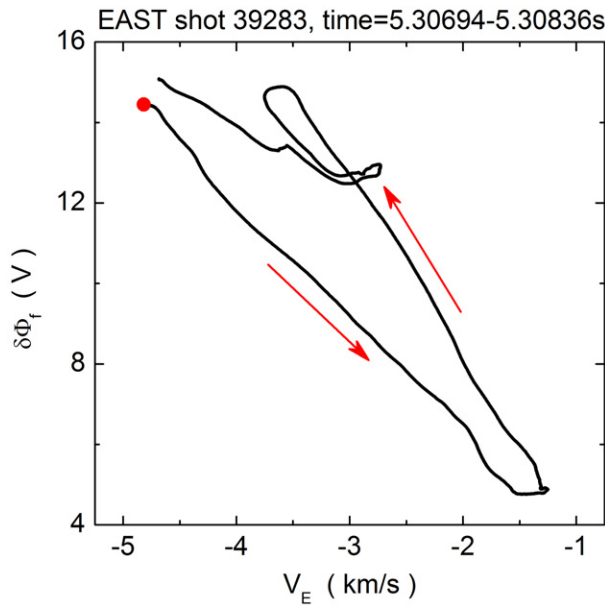


Figure 11. The trajectory of the system in the phase space of $E \times B$ flow velocity vs. fluctuation envelope of the inner tip during the first limit cycle.

phase space of V_E versus. fluctuation envelope is shown in figure 11. The fluctuation envelope of the inner tip during the first limit cycle in figure 10 is plotted as a function of V_E , which shows a limit cycle rotating in the counter-clockwise

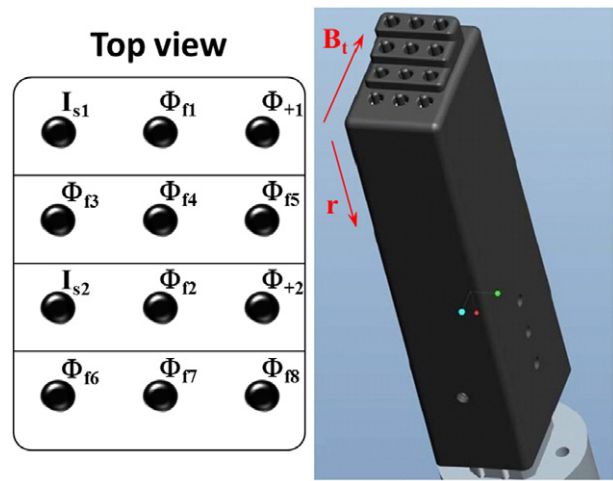


Figure 12. Layout of the 3×4 probe array.

direction. It indicates that the fluctuation suppression and recovery slightly leads the V_E change, which may suggest that the change in V_E and floating potentials is a consequence of the fluctuation change. This causality is consistent with the picture of turbulence-driven flow, in which the turbulence suppression leads to the loss of driving force for the flows, and in turn, the flows decay in response to the turbulence suppression. This relationship between fluctuation intensity and $E \times B$ velocity is consistent with the so-called type-Y LCOs, in which the turbulence intensity leads the $E \times B$ flow, observed recently in DIII-D [39] during the L–I–H transition and in HL-2A [41, 59] during the L–I–L transition or at the beginning of the L–I–H transition.

During the L–I–L transition, the global confinement may still be in L-mode, as there is no significant increase in either the stored energy (figure 9(d)) or the global confinement time, however, the local radial pressure gradient near the separatrix is significantly steepened after fluctuation suppression, according to our GPI measurements [40]. The steepened local gradient may lead to the recovery of turbulence level, and then the growing turbulence reinitiates the flow drive.

5. L–I–H transition slightly inside the separatrix

A 3×4 probe array has been used to study the dynamics of the L–I–H transition with three tips spaced by $dp = 6$ mm along the poloidal direction and four layers of tips spaced by $dr = 2.5$ mm in the radial direction, facing the plasma current in the toroidal direction, as shown in figure 12. Each tip is 2 mm in length and 2 mm in diameter. Both the probe head and the tips are made of graphite. The arrangement of the tips in this experiment is shown in figure 12. The three tips in the first and third layers are operated as triple-probes to provide the time-dependent measurements of electron density, electron temperature and plasma potential, at two radial locations separated radially by $L_r = 2dr = 5$ mm. The other tips are used to measure floating potentials. The electron temperature is calculated as $T_e = (\Phi_+ - \Phi_f)/\ln 2$, where Φ_+ is the potential measured by the positively biased tip. The plasma potential is $\Phi_p = \Phi_f + \alpha T_e$. The electron density is estimated as $n_e = I_s / (0.5eA_{\text{eff}}C_s)$, where $C_s = (2T_e/m_i)^{1/2}$ is the sound

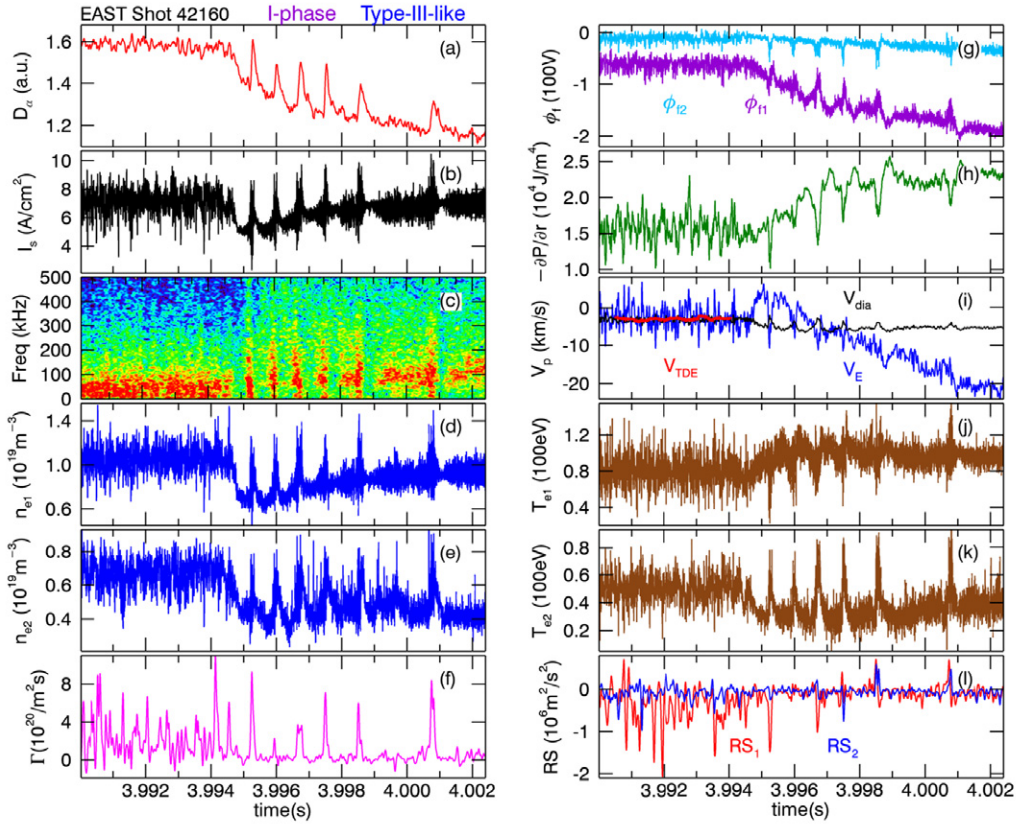


Figure 13. The time history of (a) divertor $D\alpha$ emission, (b) ion saturation current from the innermost tip, (c) its power spectrum, (d) electron density at $\Delta r \sim -5$ mm, (e) electron density at $\Delta r \sim 0$ mm, (f) fluctuation-driven particle flux at $\Delta r \sim -5$ mm, (g) floating potentials, Φ_{f1} at $\Delta r \sim -5$ mm and Φ_{f2} at $\Delta r \sim 0$ mm, (h) electron pressure gradient, (i) $E \times B$ flow velocity (blue), electron diamagnetic drift velocity (black) and poloidal phase velocity of fluctuations (red), (j) electron temperature at $\Delta r \sim -5$ mm, (k) electron temperature at $\Delta r \sim 0$ mm, (l) turbulent Reynolds stresses, RS_1 at $\Delta r \sim -5$ mm (red) and RS_2 at $\Delta r \sim 0$ mm (blue).

speed, A_{eff} is the effective collecting area of the tip, I_s is the ion saturation current and $e = 1.602 \times 10^{19}$ C. Here, we assume that the ion temperature is equal to the electron temperature, $T_i = T_e$, in calculating the sound speed, as there is no measurement of T_i . The electron pressure can be evaluated as $p_e = n_e T_e$.

The L–I–H transitions have been captured in several shots by the probe array in this experiment. The observations are generally similar, so that only one shot, No 42160, is presented here. The results are shown in figure 13. It is a typical shot for the L–I–H transition with USN configuration (favourable ion ∇B direction with ‘reversed B_t ’), as shown in figure 2, at marginal power with $\bar{n}_e = 2.3 \times 10^{19} \text{ m}^{-3}$. The total source power, i.e. with $P_{\text{LHCD}} = 1.5$ MW, $P_{\text{ICRF}} = 0.9$ MW, $P_{\text{ohmic}} = 0.2$ MW ($I_p = 0.4$ MA), is considerably higher than the threshold power (~ 1 MW) with DN configuration under the same conditions. The L–H transition is induced by a slight increase of the LHCD power from 1.4 to 1.5 MW.

In this shot, the probe array captured an L–I–H transition when it stopped at a radial location with the innermost layer of tips at ~ 5 mm inside the separatrix. The duration of I-phase with USN configuration is usually very short in time, with only a few limit cycles, as shown in figure 13(a). The amplitude of limit cycles in the divertor $D\alpha$ emissions is smaller than those with DN configuration. The duty cycle is typically $\tau_L/\tau_H < 1$, with τ_H increasing progressively as approaching

the H-mode. In addition, during the I-phase the cycle-averaged $D\alpha$ level gradually decreases with time, which may suggest a progressive enhancement in particle confinement towards the H-mode.

Experimentally, the type III ELMs, which also occur close to the power threshold, can be distinguished from the LCOs by the occurrence of the precursor oscillations, as discovered in the early experiments on ASDEX [6]. Figures 13(b) and (c) show the raw signal of the ion saturation current from the innermost tip, I_{s1} , and its time-dependent power spectrum. A precursor oscillation at ~ 100 kHz can be seen preceding the last two spikes in the divertor $D\alpha$ emission signal. They are therefore type III ELMs. The four spikes in front of them are limit cycles, since there is no detectable precursor oscillation. It is frequently seen during the L–I–H transition, especially during a slow power ramp-up [19, 20], a gradual change from the LCOs that appear right following the L–I transition without detectable precursor oscillation to the type III ELMs before the ELM-free phase where clear precursor activity is seen. Furthermore, the LCOs usually appear immediately following the L–I transition, however, the first type III ELM typically appears either after a short ELM-free phase during which the pedestal builds up as shown in figures 3 and 9, or changes smoothly from the LCOs as seen in this case.

The fluctuation levels are strongly suppressed in the whole frequency domain during the quiescent period in each limit

cycle, leading to an exponential decay typically of hundreds of μs in the divertor D_α emissions and SOL electron density, n_{e2} , (figure 13(e)), electron temperature, T_{e2} , (figure 13(k)). However, meanwhile the electron temperature, T_{e1} , measured at ~ 4 mm inside the separatrix (figure 13(j)) increase during the quiescent period. It indicates a steepening of the local T_e gradient near the separatrix. The T_e gradient is then flattened by the transient enhancement of turbulent fluctuations, as indicated by the negative spikes in T_{e1} and positive spikes in T_{e2} . The electron density, n_{e1} , measured at ~ 4 mm inside the separatrix (figure 13(d)) does not behave like T_{e1} . It decreases during the quiescent period, which indicates that only a T_e barrier rather than a n_e barrier forms near the separatrix or the n_e barrier may be located at an even deeper position.

Broadband fluctuations (mainly in 0–200 kHz, broader than those in the L-mode) are observed during the transient enhancement period in each limit cycle as seen in figure 13(c), indicating that the recovery of fluctuation level in the I-phase is due to the transient enhancement in turbulence rather than driven by a coherent MHD mode, like ELMs. The timescale for the fluctuation growth at the transient enhancement is typically within 100 μs , which is as short as the timescale for the fluctuation suppression at the L–I or L–H transitions. Significant outward particle flux, $\Gamma = \langle \delta v_{r1} \delta n_{e1} \rangle$, is driven by the transient enhancement of turbulent fluctuations as shown in figure 13(f), which transiently even exceeds the L-mode flux level. Here, the radial advection velocity fluctuation is estimated as $\delta v_{r1} = \delta E_{p1}/B = (\delta \Phi_{f4} - \delta \Phi_{f3})/(d p B)$. The fluctuations appear to transport particles and heat into the SOL, leading to the positive spikes in the SOL electron density, n_{e2} , and electron temperature, T_{e2} , and the periodic flattening of the local electron pressure gradient at the plasma edge as shown in figure 13(h). Here, the electron pressure gradient is estimated as $-\partial p_e/\partial r = (p_{e1} - p_{e2})/L_r$. The mean value of the electron pressure gradient increases progressively from one limit cycle to another, suggesting a continuous buildup of the pedestal during the I-phase, then saturates when the transition into the type III ELMs occurs.

Figure 13(g) shows the floating potentials, Φ_{f1} , measured at ~ 5 mm inside the separatrix and, Φ_{f2} , near the separatrix. Φ_{f1} drops significantly towards the negative direction during the I-phase, while Φ_{f2} is only slightly reduced, which gives rise to an increasing radial gradient of the floating potential at the plasma edge.

Figure 13(i) shows the $\mathbf{E} \times \mathbf{B}$ flow velocity, $V_E = E_r/B$, the electron diamagnetic drift velocity, $V_{\text{dia}} = (\partial p_e/\partial r)/(e B n_e Z_{\text{eff}})$, and the poloidal phase velocity of fluctuations in the laboratory frame estimated from the cross correlation between the floating potentials (Φ_{f3} , Φ_{f4} and Φ_{f5}) based on the time-delay estimation (TDE) technique [60, 61], V_{TDE} . Here, note that the contribution from the radial T_e gradient has been taken into account in calculating the radial electric field, $E_r = (\Phi_{p1} - \Phi_{p2})/L_r$. The local magnetic field at the outer midplane is $B \sim 1.46$ T and $Z_{\text{eff}} \sim 2$. In the L-mode before the transition, the three velocities, V_E , V_{dia} and V_{TDE} , are all in the electron diamagnetic drift direction, i.e., negative in the figure, and very close to each other, indicating that the fluctuations may have a very small phase velocity in the plasma frame in comparison to the $\mathbf{E} \times \mathbf{B}$ velocity. At the first L–I transition, V_E changes towards the ion diamagnetic drift

direction, consistent with the observation at the single-step L–H transition (figure 8(b)) and the L–I–L transition (figure 10(c)), although the contribution from the radial T_e gradient is neglected in the previous V_E calculation. The transient enhancement of turbulent fluctuations drives V_E in the electron diamagnetic drift direction, as seen in figure 13(i). This observation is consistent with the GPI measurements inside the separatrix in EAST [40]. The poloidal velocity from the GPI diagnostic is the phase velocity of fluctuations, estimated based on a modified TDE technique.

During the I-phase, the mean value of V_E drops continuously towards the negative direction, which is mainly due to the significant drop in the floating potential, Φ_{f1} . It does not follow the time evolution of the electron diamagnetic drift velocity, V_{dia} . The deviation of V_E from V_{dia} may suggest that there are significant perpendicular flows or the ion pressure gradient evolves significantly differently from the electron pressure gradient.

Figure 13(l) shows the turbulent Reynolds stresses at two radial locations, calculated as $\text{RS}_1 = ((\delta \Phi_{f1} - \delta \Phi_{f4})(\delta \Phi_{f5} - \delta \Phi_{f3}))/((2d p dr B^2))$ and $\text{RS}_2 = ((\delta \Phi_{f2} - \delta \Phi_{f7})(\delta \Phi_{f8} - \delta \Phi_{f6}))/((2d p dr B^2))$. Transient enhancement in the turbulent Reynolds stress with significant amplitude, i.e., $\sim 1 \times 10^6 \text{ m}^2 \text{ s}^{-2}$, which is comparable to the L-mode level, has been observed during the I-phase. The turbulent Reynolds stress at the inner location, RS_1 , appears to be much higher than that at the outer location, RS_2 , indicating a significant radial gradient. Here, the radial distance between RS_1 and RS_2 is $L_r = 2dr = 5$ mm. Negative Reynolds stress is observed in the L-mode and the I-phase, i.e., in the first four cycles. However, positive Reynolds stress is observed for the last two spikes, which is thought to be associated with the type III ELMs. Here, the negative Reynolds stress corresponds to kinetic energy transfer from the turbulence into the $\mathbf{E} \times \mathbf{B}$ flows, hence driving the flows; while the positive Reynolds stress corresponds to kinetic energy transfer from the flows back to the turbulence, thus damping the flows, i.e., acting as ‘turbulent viscosity’. The transition from the LCOs to the type III ELMs occurs approximately when V_E crosses V_{dia} , as shown in figure 13(i).

In addition, a small-amplitude limit cycle appears prior to the L–I transition at 3.9945 s, as shown for instance in figure 13(b), where one can see that the fluctuation level is transiently suppressed, however the suppression is not as strong as that during the normal LCOs. An associated small dip can also be seen in the divertor D_α emission. Bursts in the particle flux are seen just before and after the transient suppression period. Such small-amplitude LCOs with a single or a few cycles are frequently seen prior to the I-phase or single-step L–H transition near the power threshold [32], acting like a transition precursor. They share similar features of the normal LCOs, as confirmed by the GPI measurements in EAST [40]. More details will be presented in section 8.

6. L–I–H transition in the SOL

More information about the L–I–H transition in the SOL was obtained with a 12-tip probe array. Figure 14 shows the arrangement of the tips. Each tip is 2 mm in length and 2 mm in diameter. It is composed of two layers of four-tip

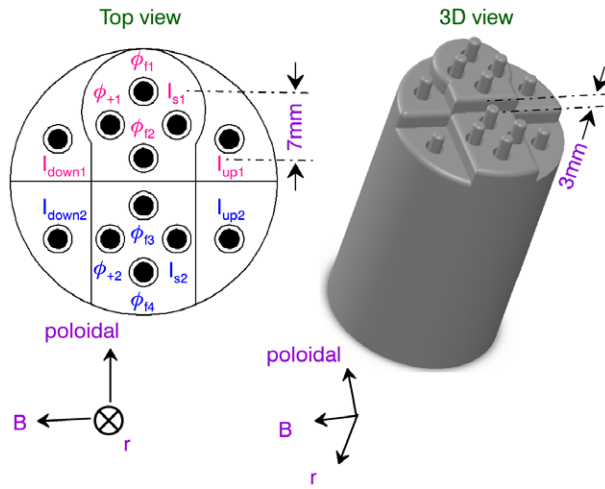


Figure 14. Layout of the 12-tip probe array.

probe array and Mach probes, radially separated by $dr = 3$ mm, to provide the time-dependent measurements of electron density, electron temperature, plasma potential and parallel ion flow velocities simultaneously. The tips are arranged like this to avoid shading each other in the direction along the magnetic field lines. Taking the first layer as an example, the electron temperature and the plasma potential are calculated as $T_{e1} = (\Phi_{+1} - \Phi_f)/2$ and $\Phi_{p1} = \Phi_f + \alpha T_{e1}$, respectively, where the average, $\Phi_f = (\Phi_{f1} + \Phi_{f2})/2$, is approximately the floating potential at the midpoint of Φ_{f1} and Φ_{f2} . The two floating potentials are poloidally separated by $d\rho = 7$ mm. The electron density is estimated as $n_{e1} = I_{s1}/(0.5eA_{\text{eff}}C_{s1})$. The Mach probes are used to measure parallel ion flow velocities with the upstream and downstream tips aligned with the local magnetic field lines. The parallel Mach numbers are estimated from the ratio of the upstream and downstream ion saturation currents, $M_{\parallel} = 0.4 \ln(I_{\text{up}}/I_{\text{down}})$ [56, 57]. The parallel ion flow velocity is then estimated as $V_{\parallel} = M_{\parallel} C_s$. The probe head is too big to be inserted across the separatrix due to serious disturbance to the edge plasma, which tends to prevent or delay the onset of the L–H transition. Therefore, transition data from this probe array is only available in the SOL up to the separatrix location.

Several shots with the L–I–H transitions have been captured by the probe. The phenomena are similar, so only one shot, No 40844, is presented here. It is a typical shot with the L–I–H transition with DN configuration, heated by 1.2 MW LHCD, 0.5 MW ICRF and ~ 0.2 MW ohmic power with $I_p = 0.4$ MA and $\bar{n}_e = 2.4 \times 10^{19} \text{ m}^{-3}$ at the transition. In this shot, the probe reached a radial position with the innermost tips at ~ 3 mm outside the separatrix and stayed there for ~ 100 ms, during which the probe captured an L–I–H transition. The tips on the second layer are at ~ 6 mm outside the separatrix.

During the I-phase at the L–I–H transition, i.e., 2.603–2.632 s, the central-line-averaged density and the plasma-stored energy ramp-up as shown in figure 15, suggesting that the global particle and energy confinements are improved. Meanwhile, the radial gradient in the XUV radiations at the plasma edge gradually increases, indicating that the edge pedestal is building up. In contrast, there is no

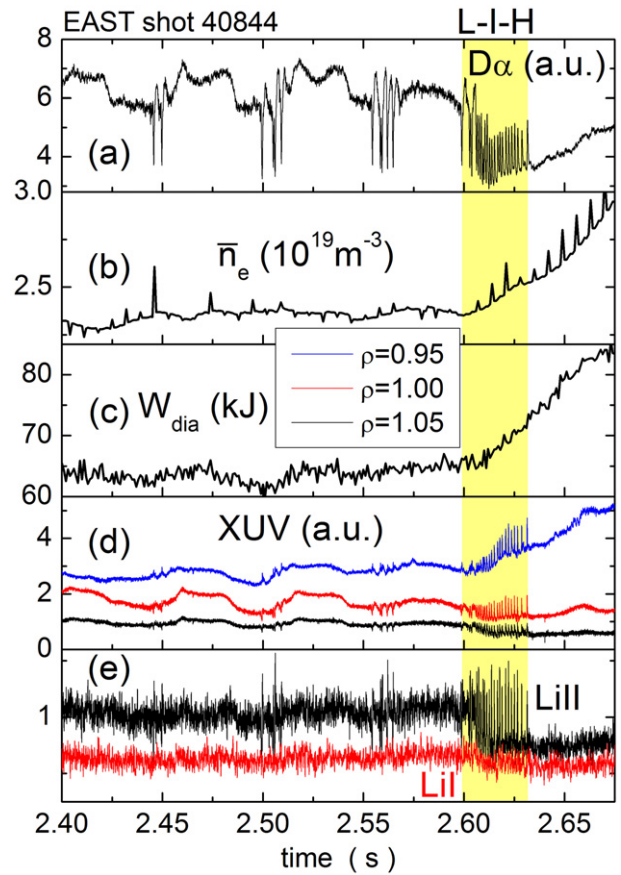


Figure 15. The time history of (a) divertor $D\alpha$ emission, (b) central-line-averaged density, (c) plasma-stored energy from the diamagnetic measurement, (d) XUV radiations at the plasma edge, $\rho = 0.95$ blue, 1.00 red and 1.05 black, (e) Li I (red) and Li II (black) line emissions from the plasma edge near the inner midplane.

clear change in the central-line-averaged density, the plasma-stored energy or the XUV radial gradient during the L–I–L transitions, as shown in figures 15 and 9. This is an important distinction between the L–I–H and the L–I–L transitions, which may suggest that a gradual buildup of the edge pressure gradient during the I-phase leads to the final transition into the H-mode; otherwise, the plasma returns to the L-mode. In addition, the oscillations associated with the LCOs are seen in the Li II line emission but very weak in the Li I line emission, as shown in figure 15(e), suggesting that the oscillations are rather weak in the far SOL, since the Li I line emission is predominantly from the low- T_e region ($T_e < 20$ eV), while the Li II line emission is mainly from the vicinity of the separatrix where T_e is relatively higher. The Li I and Li II line emissions were measured by a monochromator viewing the high-field-side plasma edge near the inner midplane [62].

The I-phase at the L–I–H transition starts with two isolated limit cycles near 2.603 s, as indicated in the divertor $D\alpha$ emission signal (figure 16(a)), followed by a series of limit cycles with increasing duration of the quiescent period, τ_H , and decreasing duty cycle (evolves from $\tau_L/\tau_H \sim 1$ to $\tau_L/\tau_H \ll 1$) as approaching the H-mode. A transition into an ELM-free H-mode phase occurred at 2.632 s. The quiescent period τ_H , i.e. the time intervals between two adjacent pulses τ_{interval} , are shown in figure 16(h). It generally increases with

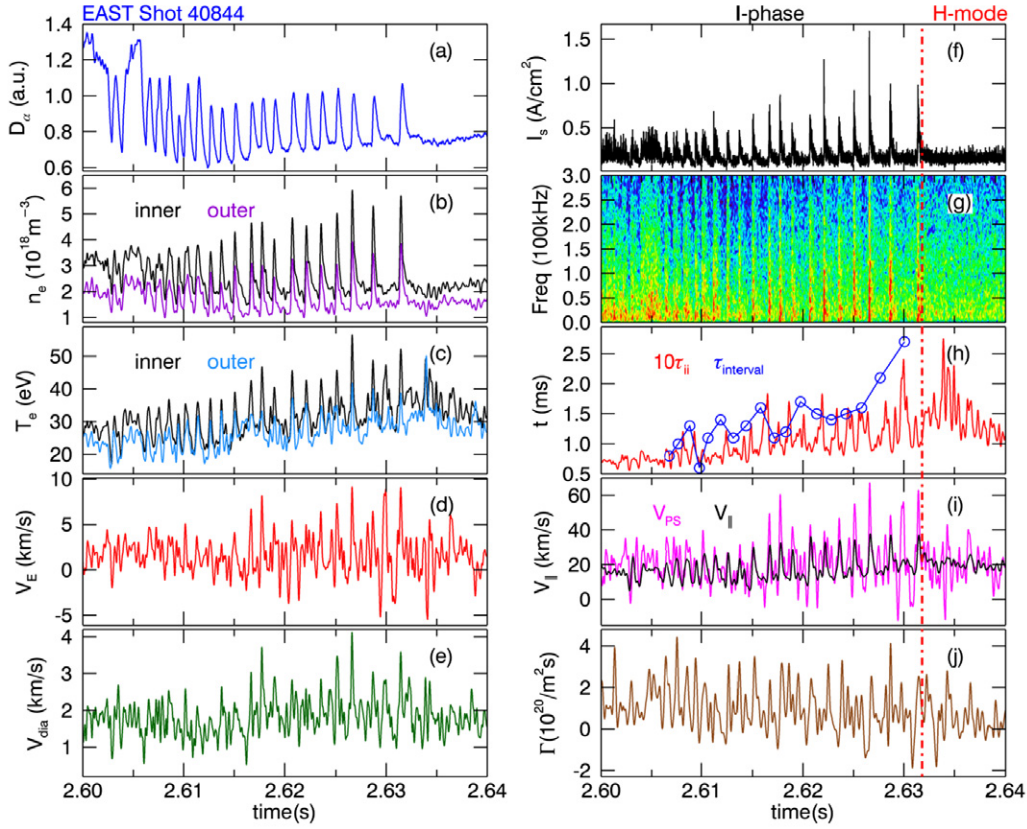


Figure 16. The time history of (a) divertor $D\alpha$ emission, (b) electron densities measured at $\Delta r \sim 3$ mm (black) and $\Delta r \sim 6$ mm (purple), (c) electron temperatures measured at $\Delta r \sim 3$ mm (black) and $\Delta r \sim 6$ mm (blue), (d) $\mathbf{E} \times \mathbf{B}$ flow velocity, (e) ion diamagnetic drift velocity, (f) ion saturation current at $\Delta r \sim 3$ mm, (g) its power spectrum, (h) ten times of the ion–ion collision time (red) and time intervals between two adjacent pulses (blue), (i) parallel ion flow velocity (black) and P–S flow velocity (pink), (j) fluctuation-driven particle flux.

time. The ion–ion collision time, τ_{ii} , calculated with the SOL local parameters, also increases as approaching the H-mode. However, it is more than 10 times smaller than the time interval, τ_{interval} . The plasma edge near the separatrix is typically in the plateau regime, where the flow damping rate is controlled by the transit frequency $\omega_t = v_{\text{thi}}/q_{95}R_0$ and $\gamma_{\text{damp}} \approx \omega_t \varepsilon^{1/3}$ [63], where $\varepsilon = a/R_0$. This timescale is also shorter than the time interval between adjacent pulses. Thus, the above timescale estimation suggests that the LCO frequency may not be determined by the flow damping rate.

Figures 16(f) and (g) show the raw signal of ion saturation current, I_{s1} , and its time–frequency power spectrum, respectively. Broadband fluctuations (mainly in 0–200 kHz) are seen during the transient enhancement in each limit cycle. The I_{s1} decays exponentially following each transient enhancement. The decay is on the same timescale of the SOL parallel particle transport, $\tau_{||} = L_{||}/V_{||} \sim 500 \mu\text{s}$, where $L_{||} \sim 10$ m is the SOL parallel connection length and $V_{||} = M_{||}C_s \sim 20$ km s^{-1} is the SOL parallel ion flow velocity (figure 16(i)).

Positive spikes in n_e and T_e are seen in the SOL with increasing amplitudes as approaching the H-mode, as shown in figures 16(b) and (c). The pulse amplitude appears to be smaller at a radial position away from the separatrix, which gives a radial gradient in n_e and T_e . The transient enhancement in the SOL n_e and T_e is induced by the enhanced cross-field turbulent transport of particles and heat, as confirmed by the

direct measurement of the turbulence-driven radial particle flux with the four-tip probe array. Significant outward particle flux, $\Gamma = \langle \delta v_{r1} \delta n_{e1} \rangle$, is observed, driven by the transient enhancement of turbulent fluctuations, as indicated by the positive spikes in figure 16(j). Here, the radial advection velocity fluctuation is estimated as $\delta v_{r1} = \delta E_{p1}/B = (\delta \Phi_{f1} - \delta \Phi_{f2})/(d\rho B)$.

The $\mathbf{E} \times \mathbf{B}$ flows, $V_E = E_r/B$, and diamagnetic flows, $V_{\text{dia}} = (-\partial p_e/\partial r)/(eBn_e Z_{\text{eff}})$, in the ion diamagnetic direction, are enhanced during the transient enhancement of turbulent fluctuations as shown in figures 16(d) and (e). The spikes appear to be correlated with each other and comparable in amplitude, however, the $\mathbf{E} \times \mathbf{B}$ flows cannot be balanced by the ion diamagnetic flows in the radial force balance, since they are both in the ion diamagnetic direction. Here, note that the contribution from the radial T_e gradient has been taken into account in the radial electric field calculation, $E_r = (\Phi_{p1} - \Phi_{p2})/dr$. The electron pressure gradient is estimated as $\partial p_e/\partial r = (p_{e2} - p_{e1})/dr$. The positive excursions of the $\mathbf{E} \times \mathbf{B}$ flows in figure 16(d) during the observed intermittent turbulent bursts are predominantly due to the increased radial T_e gradient, i.e., essentially the increased sheath potential. The contribution from the radial gradient of the floating potential is relatively small. Usually, the sheath boundary condition in the SOL introduces a strong momentum sink to the momentum balance equation, which damps the turbulence driven flows, so that the plasma potential is largely tied down to the sheath potential [64].

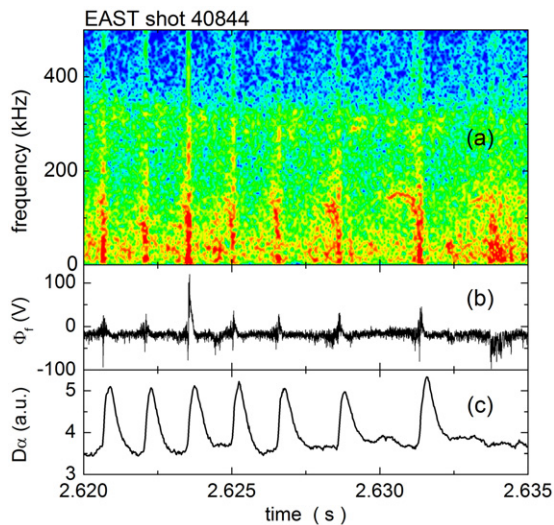


Figure 17. The time history of (a) power spectrum of the floating potential at the separatrix, (b) floating potential, (c) divertor $D\alpha$ emission.

Furthermore, significant parallel flows in the co-current direction, up to 50 km s^{-1} , are observed during the transient enhancement of turbulent fluctuations, and the parallel flow velocity measured by the Mach probe, V_{\parallel} , is found to be strongly correlated with the Pfirsch–Schlüter (P–S) flow velocity at the outer midplane, V_{PS} , as shown in figure 16(i). It may suggest that the parallel flow at the outer midplane is dominated by the P–S flow. Here, the P–S flow velocity is calculated as $V_{PS} = 2r[E_r - (\partial p_e / \partial r) / (en_e)] / (R_0 B_p)$ [57], where B_p is the strength of the local poloidal magnetic field. E_r and $(-\partial p_e / \partial r)$ have comparable contributions to the transient enhancement in the P–S flows during the I-phase.

Another four-tip probe array was mounted on the other reciprocating probe system, reached right at the separatrix. Figure 17 shows one channel of floating potential signal and its time–frequency power spectrum. As one can see, a precursor oscillation at a frequency of $\sim 150 \text{ kHz}$ only appears preceding the last two spikes, which characterizes the type III ELMs. The quiescent periods, τ_H , prior to the last two spikes appear to be longer than those in the preceding LCOs. There is a gradual change from the LCOs to the type III ELMs. The precursor oscillation appears to chirp down in frequency right before the ELM crash, which is mainly due to the Doppler shift introduced by the rotation breaking effect [65]. In addition, the precursor oscillation can only be seen by the probe tips inside or near the separatrix, and cannot be detected by the probe tips in the SOL, as shown in figure 16(g), suggesting that the precursor oscillations are present mainly in the closed field line region. The behaviours of electron density and temperature measured by the four-tip probe array at the separatrix are similar to those measured by the 12-tip probe array in the SOL, i.e., exhibiting positive spikes.

In addition, the previous study on ASDEX Upgrade concluded that no LCO occur with the unfavourable ion ∇B direction, either at the L–H forward transition or the H–L back transition [9]. However, the EAST experiments show that the I-phase can be observed both at the L–H transition and at the H–L transition with the unfavourable ion ∇B direction,

but much less frequently than those with DN configuration, typically with much shorter I-phase duration. Figure 18 shows a typical example for the H–L back transition via a short I-phase with the unfavourable ion ∇B direction, i.e., LSN configuration with $dR_{sep} = -1.5 \text{ cm}$ in this case. The first two spikes in the divertor $D\alpha$ emission signal are type III ELMs, since precursor oscillations can be seen in the power spectrum of magnetic fluctuations measured by the fast Mirnov coils located on the low-field side as shown in figure 18. The H–L back transition revisits the path at the forward transition with a gradual change from the type III ELMs to the LCOs. The pedestal pressure gradient is progressively reduced during the I-phase as indicated by a gradual decrease in the radial gradient of the XUV radiations in figure 18(c). The amplitude of LCOs and the quiescent period, τ_H , also gradually decrease. I-phases with similar behaviours also appear at the H–L back transition with the favourable ion ∇B direction.

7. Magnetic perturbations

Significant magnetic perturbations associated with the LCOs during the I-phase have been detected by the Mirnov coils located on the chamber wall. The magnetic signal shown in figure 19(b) is measured by the No 7 Mirnov probe, which is located at the top, behind the upper divertor dome. The coil is oriented to measure the poloidal magnetic perturbations, δB_p , with the effective area of 0.17 m^2 . The distributions of the Mirnov coils are shown in figure 20. The RMS amplitude of the magnetic perturbations measured at this location is $|\delta B_p| \sim 1 \text{ G}$ (corresponding to $|dB_p/dt| \sim 1 \text{ T s}^{-1}$), which is about $|\delta B_p|/B_p \sim 0.06\%$ of the background poloidal magnetic field at the outer midplane. Shot 38813 is a typical discharge at marginal power with DN configuration, heated by 0.9 MW LHCD, 0.9 MW ICRF and $\sim 0.3 \text{ MW}$ ohmic power with $I_p = 0.4 \text{ MA}$.

Figure 19 shows an H–L back transition at 8.339 s, followed by a single limit cycle at 8.344 s and two L–I–L transitions, with a final L–I–H transition starting at 8.435 s. The isolated spike at 8.260 s is a type III ELM. As can be seen in figure 19(b), the amplitude of the magnetic perturbations associated with the LCOs is comparable to those of the type III ELMs. The I-phase at the H–L back transition has been studied previously on ASDEX Upgrade [9], showing similar behaviour to the I-phase at the L–H forward transition or L–I–L transition. They exhibit similar oscillation frequency, i.e., $\sim 1 \text{ kHz}$ in this shot as shown in figure 19(c). For the H–L back transition, the oscillation frequency increases as approaching the L-mode. For the L–I–H transition, the oscillation frequency is significantly reduced as approaching the transition into the ELM-free H-mode, which is mainly due to an extension in the duration of the quiescent period, τ_H . For the L–I–L transitions, the oscillation frequency slightly decreases with time during the I-phase. The amplitude of the magnetic perturbations generally increases with decreasing oscillation frequencies.

Figure 20 shows the magnetic perturbations (dB_p/dt) at the beginning of the L–I–H transition, i.e., in the time window $t_4 = 8.435\text{--}8.442 \text{ s}$, measured by two poloidal arrays of Mirnov coils, toroidally separated by 180° , i.e., one near port C (CMPT) and the other near port K (KMPT). The magnetic

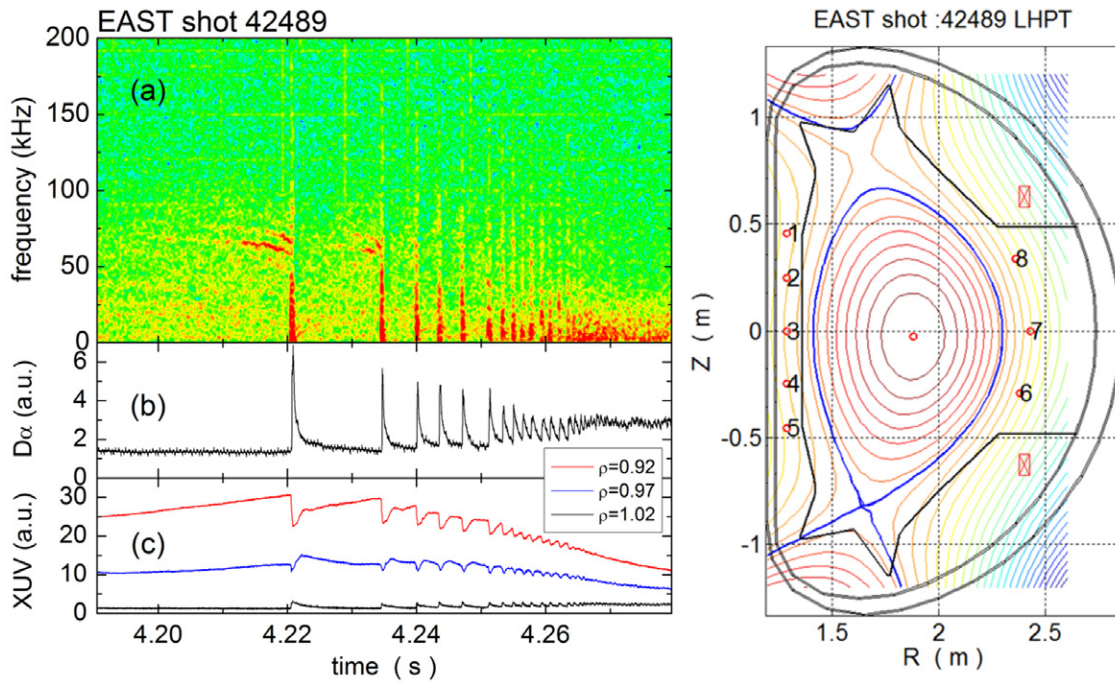


Figure 18. The time history of (a) power spectrum of magnetic fluctuation measured by the No. 8 fast Mirnov coils located on the low-field side, (b) divertor $D\alpha$ emission, (c) XUV radiations at the plasma edge, $\rho = 0.92$ red, 0.97 blue and 1.02 black. The right plot shows the plasma configuration at 4.26 s and the distribution of the fast Mirnov coils.

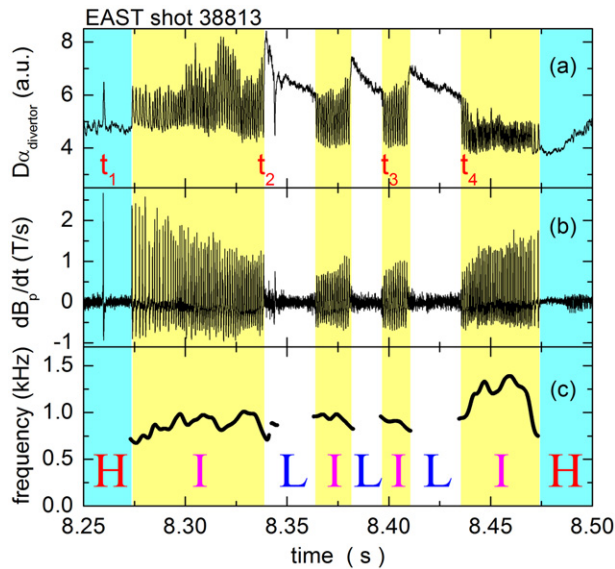


Figure 19. The time history of (a) divertor $D\alpha$ emission, (b) magnetic signal measured by the No 7 Mirnov probe, (c) oscillation frequency based on Fourier analysis.

perturbations have been normalized to their root-mean-square (RMS) values. The divertor $D\alpha$ emission signal is also displayed, at the top of the plot. Comparing the magnetic perturbations between the two arrays, one can see that the magnetic perturbations are nearly in phase for all poloidal positions, suggesting that the magnetic perturbations are axisymmetric in the toroidal direction, i.e., the toroidal mode number is $n = 0$. It is further confirmed by the measurements

from a toroidally distributed Mirnov probe array, which is composed of 16 probes. In the poloidal direction, they appear to be dominated by an $m = 1$ component, with nearly up-down anti-phase. However, there is a smooth phase transition from above to below the midplane. Similar $m/n = 1/0$ magnetic perturbations have also been observed recently during the I-phase in the HL-2A tokamak [41].

The magnetic perturbations associated with the type III ELMs are typically stronger than those for the LCOs and exhibit similar spatial structures, i.e., $n = 0$ and poloidally dominated by an $m = 1$ component, as shown in figure 21, in the time window $t_1 = 8.258$ – 8.262 s. However, they appear to have much stronger skewness relative to those for the LCOs, nearly in phase on the low-field side.

Figure 21 also shows the magnetic perturbations just before the H–L back transition, i.e., in the time window $t_2 = 8.335$ – 8.339 s, and at the beginning of the L–I–L transition, i.e., in the time window $t_3 = 8.396$ – 8.400 s. There is not much difference in comparison with those during the L–I–H transition. In addition, one may notice that there are two small-amplitude limit cycles at the beginning of the L–I–L transition in the time window t_3 , acting like a precursor to the L–I transition. The magnetic perturbations associated with these two small-amplitude limit cycles also exhibit similar magnetic structure, albeit much smaller in amplitude.

One possible generation mechanism for such magnetic structure is the periodic buildup and collapse of the edge transport barrier during the I-phase due to a modulation in the turbulence level and cross-field transport at the plasma edge, which may lead to current perturbations in response to the pressure gradient perturbations to maintain the MHD radial force balance, $\nabla p = j \times B$ [41]. The $m = 1$ magnetic component could be associated with the P–S current.

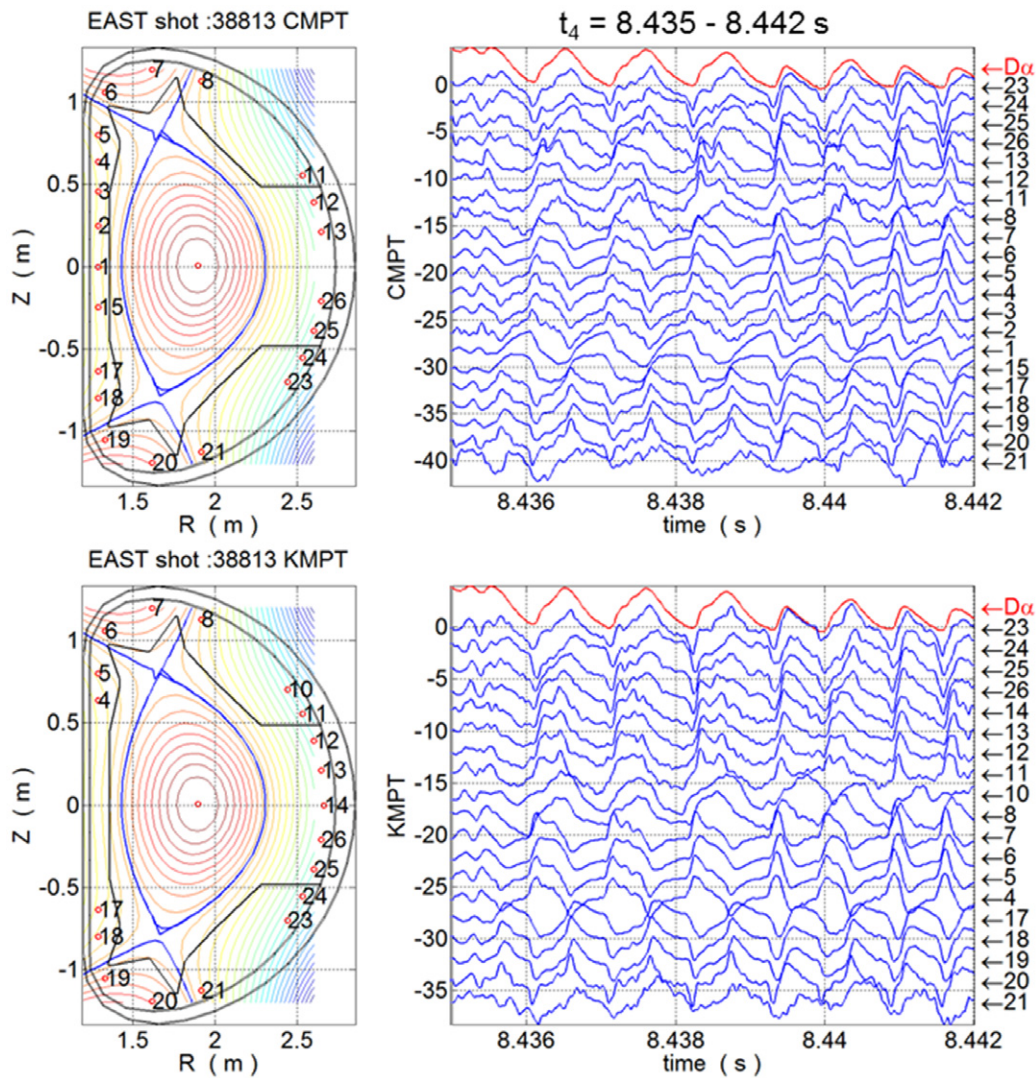


Figure 20. The distribution of two poloidal arrays of Mirnov coils toroidally separated by 180° , i.e., one near port C (CMPT) and the other near port K (KMPT). The time history of magnetic perturbations (dB_p/dt) at the beginning of the L–H transition, i.e., in the time window $t_4 = 8.435\text{--}8.442$ s, measured by the Mirnov coils. The red curves show the divertor $D\alpha$ emission.

8. Small-amplitude LCOs

In EAST, there is another type of LCOs with much smaller amplitude and/or higher frequency (up to 4 kHz), compared with the normal LCOs, which appears in the $D\alpha$ emission signals preceding a clearly defined single-step H-mode transition, acting like a transition precursor, or mixed with normal LCOs. We call them ‘small-amplitude LCOs’. Observation of the small-amplitude LCOs in EAST has been reported recently [32], showing that it appears hundreds of ms before the L–H transitions or after the H–L back transitions when the input heating power is marginal to the transition threshold. Similar small-amplitude LCOs have been observed previously in NSTX [27] and C-Mod [35] with GPI diagnostic, in JFT-2 M with HIBP [42] and recently in ASDEX Upgrade with a scanning probe near the lower X-point [66]. The small-amplitude LCOs are usually less regular in frequency and amplitude than the normal LCOs, but exhibit similar features of turbulence-flow interactions at the plasma edge [32].

The LCOs appearing in the 2010 EAST experimental campaign were mostly small-amplitude LCOs and the L–H

transitions are mostly single-step L–H transitions even the input power was very marginal to the transition threshold, as reported in reference [32]. However, the normal LCOs prevail in the 2012 EAST experimental campaign [40]. The main difference is that the strike points on the divertor targets were placed a few centimetres away from the pumping slots in the 2012 campaign compared with the 2010 campaign in order to avoid damaging the water-cooling pipes behind the slots, which significantly reduced the divertor pumping capability. An investigation on EAST shows that the divertor pumping capability is dramatically reduced when the strike points moves 2 cm away from the pumping slots [50]. Another difference is that the wall material in the low-heat-load area, including the high-field-side wall and baffle area (except the divertor targets), was replaced from graphite to molybdenum in the 2012 campaign. However, extensive lithium wall coating with a cumulated amount of over 1 kg [47–50] was applied on EAST, which significantly reduced the exposure of the molybdenum wall to the plasma. Therefore, the difference in the wall material is unlikely the main reason for different transition

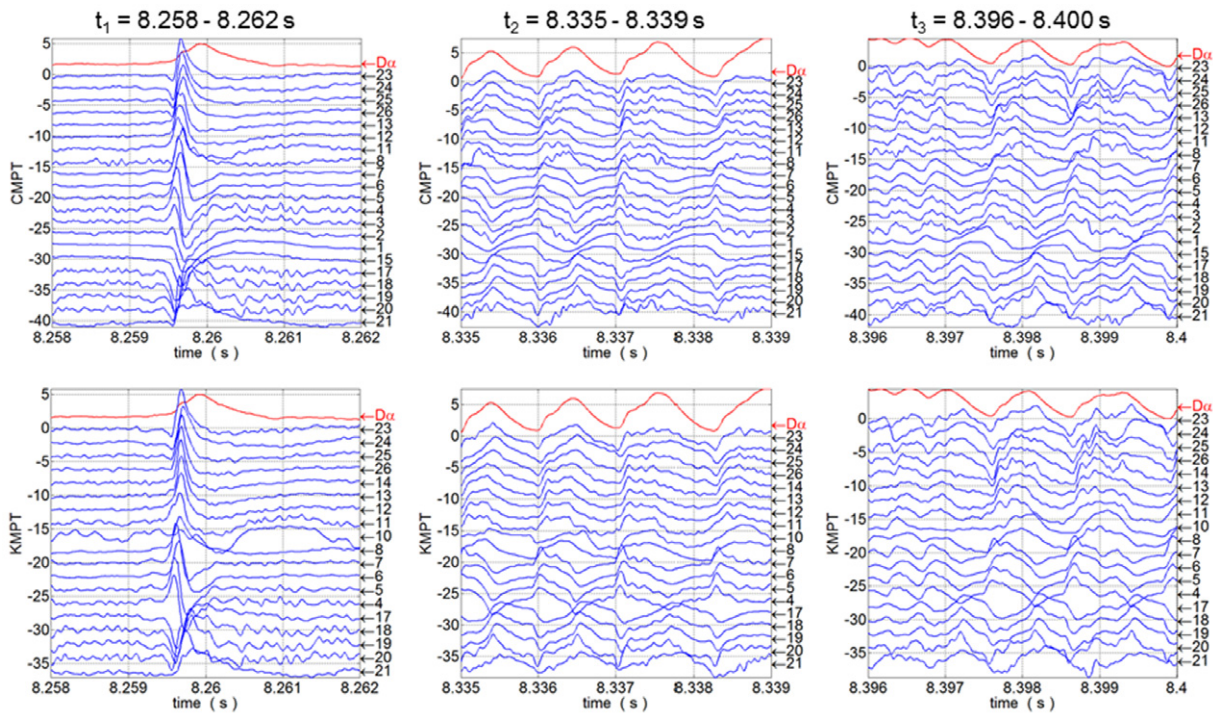


Figure 21. The time history of magnetic perturbations (dB_p/dt) measured by the Mirnov coils in two poloidal arrays toroidally separated by 180° , associated with the type III ELMs, i.e., in the time window $t_1 = 8.258\text{--}8.262$ s, just before the H–L back transition, i.e., in the time window $t_2 = 8.335\text{--}8.339$ s, and at the beginning of the L–I–L transition, i.e., in the time window $t_3 = 8.396\text{--}8.400$ s. The red curves show the divertor $D\alpha$ emission.

behaviour. In addition, in the 2012 campaign most single-step L–H transitions were obtained with LSN configuration, which strongly suggest that the divertor pumping capability is an important ingredient in determining the transition behaviour, since EAST only had one in-vessel cryopump which is located at the lower divertor [51].

Figure 22 shows a typical example for the small-amplitude LCOs with LSN configuration with $dR_{sep} = -1.5$ cm, heated by ~ 1 MW LHCD and ~ 0.4 MW ohmic power, and with $I_p = 0.62$ MA and $\bar{n}_e = 2.3 \times 10^{19} \text{ m}^{-3}$ at the transition. In this shot, there are three short ELM-free H-mode periods with single-step L–H and H–L back transitions. The H-mode periods are very short in time, since the heating power is very close to the transition threshold. A slight rise in the radiation power during the ELM-free phase leads to insufficient loss power across the plasma boundary, hence triggering the H–L back transition. Prior to each L–H transition, the small-amplitude LCOs at a frequency of ~ 2 kHz appear in the divertor $D\alpha$ emissions with a rather small-amplitude, i.e., RMS/MEAN only $\sim 3\%$, as shown in the zoom-in plot in figure 22. The magnetic perturbations associated with this small-amplitude LCOs are very weak, with $|\delta B_p| \sim 0.1$ G only, which are barely detectable in a few channels of Mirnov signals on the high-field side.

It is sometimes observed that the small-amplitude LCOs are triggered by sawtooth heat pulses, as shown in figure 23. The amplitude of the small-amplitude LCOs appears to be periodically enhanced by the sawtooth heat pulses, which are indicated by the positive pulses in the soft-x ray signal at the plasma edge. Finally, a single-step L–H transition occurs at ~ 4 ms after a sawtooth heat pulse. During this period, the amplitude of the small-amplitude LCOs continuously

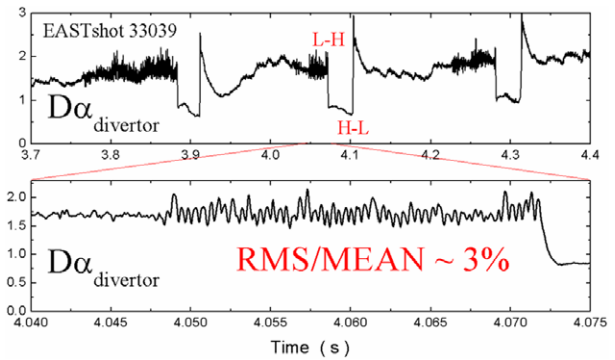


Figure 22. The time history of (a) divertor $D\alpha$ emission and (b) its zoom-in plot.

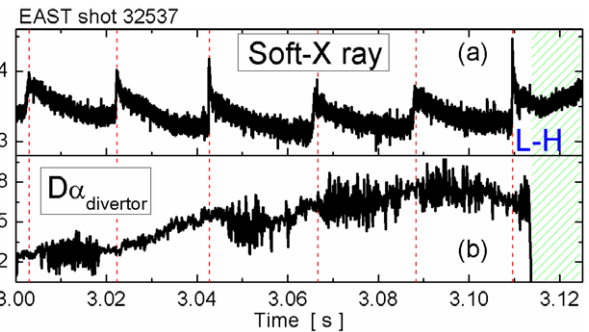


Figure 23. The time history of (a) soft-x ray at the plasma edge, (b) divertor $D\alpha$ emission.

increases. The 4 ms time delay is generally consistent with the timescale for the edge temperature gradient to build up, which can be estimated as $\tau_T = L^2/\chi_\perp$, where the cross-field thermal

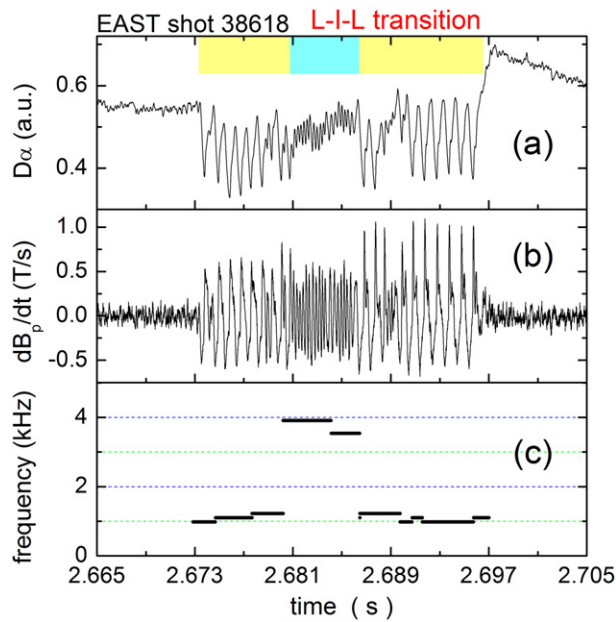


Figure 24. The time history of (a) divertor $D\alpha$ emission, (b) magnetic signal measured by the No 7 Mirnov probe, (c) oscillation frequency based on Fourier analysis.

transport coefficient at the plasma edge is $\chi_{\perp} \sim 1 \text{ m}^2 \text{ s}^{-1}$ in the L-mode just before the L–H transition and the temperature radial gradient length is $L \sim 6 \text{ cm}$.

The small-amplitude LCOs are observed to coexist with the normal LCOs in some cases. Figure 24 shows an example that the small-amplitude LCOs appear between two series of normal I-phase. The frequency of the small-amplitude LCOs ($\sim 4 \text{ kHz}$) is considerably higher than that of the normal LCOs ($\sim 1 \text{ kHz}$). The amplitude of magnetic perturbations associated with the small-amplitude LCOs is also smaller. In addition, a sharp transition from the L-mode to the I-phase is seen in this case, which is very typical with DN configuration.

9. Discussions and summary

The dynamics of the L–I–H, L–I–L and single-step L–H transitions have been studied systematically mainly based on the reciprocating probe measurements on EAST. The key findings are summarized as follows.

- (1) The appearance and behaviour of the L–I–H transition show a clear dependence on the divertor configurations and pumping capability. Most L–I–H transitions with normal LCOs were obtained with DN configuration. Most single-step L–H transitions were obtained with LSN configuration, which is normally unfavourable in terms of the ion ∇B direction on EAST. This may suggest that the divertor pumping capability is an important ingredient in determining the transition behaviour and power threshold, since EAST only had one in-vessel cryogenic pump located near the outer target of the lower divertor with a nominal pumping speed for deuterium of $\sim 75.6 \text{ m}^3 \text{ s}^{-1}$ in the 2012 campaign, which provide the main pumping. The divertor leg geometry in the lower divertor does not differ very much between the LSN and DN or USN configurations, as shown in figure 2. However, with DN or USN configurations, more particles are shunted to the upper divertor compared with the LSN configuration. Since there is no cryopump at the upper divertor, these particles cannot be effectively pumped out. Therefore, the LSN has better pumping efficiency and particle control than DN or USN configurations.
- (2) In addition to the normal LCOs, small-amplitude LCOs are observed in EAST, usually preceding a clearly defined single-step H-mode transition or sometimes coexist with the normal LCOs, exhibiting similar features of turbulence-flow interactions at the plasma edge [32]. Triggering of the small-amplitude LCOs by sawtooth heat pulses has been observed in some cases (figure 23). The LCOs observed in the 2010 campaign were predominantly small-amplitude LCOs and the L–H transitions are mostly single-step L–H transitions even with input power being very marginal to the transition threshold. However, the normal LCOs prevail in the 2012 campaign [40]. The main difference is that the strike points on the divertor targets were placed a few centimetres away from the pumping slots in the 2012 campaign, compared with the 2010 campaign, in order to avoid damaging the water-cooling pipes behind the slots. This significantly reduced the divertor pumping capability. Similar divertor configuration effects are also observed in DIII-D. The L–H transitions are more easily obtained in the low triangularity configuration, with the strike points relatively away from the pumping slots [33, 43]. Furthermore, in recent Alcator C-Mod experiments, the slot divertor configuration is associated with a lower power threshold than the vertical target configuration [67]. The outer strike point is closer to the pumping slot with the slot divertor configuration, which gives a better divertor pumping. These observations imply that weaker divertor pumping and hence a strong particle source or neutral friction [68] at the plasma edge may facilitate the access to the I-phase.
- (3) The $\mathbf{E} \times \mathbf{B}$ velocity (in the electron diamagnetic drift direction), turbulence level and turbulent Reynolds stress at $\sim 1 \text{ cm}$ inside the separatrix are observed to ramp up in the last $\sim 20 \text{ ms}$ prior to the single-step L–H transition, however, remain nearly constant near the separatrix, indicating an increase in the radial gradients at the plasma edge. The kinetic energy transfer rate from the edge turbulence to the $\mathbf{E} \times \mathbf{B}$ flows, $P_{\perp}/\langle \delta v_{\perp}^2 \rangle$, is significantly enhanced only in the last $\sim 10 \text{ ms}$ and peaks just prior to the L–H transition. The enhanced fluctuations in the last $\sim 2 \text{ ms}$ are composed of a series of intermittent spikes, which are very likely induced by a series of propagating filaments. At the L–H transition, the change in the SOL appears to lag behind that inside the separatrix by $\sim 1 \text{ ms}$, on the same time scale for fluctuation suppression, indicating that the transition initiates at a radial location inside the separatrix. The change in the SOL appears to be a consequence of the fluctuation suppression and transport reduction across the separatrix.
- (4) The $\mathbf{E} \times \mathbf{B}$ velocity measured inside the separatrix decays from typically the electron diamagnetic drift direction in the L-mode towards the ion diamagnetic drift direction in response to fluctuation suppression at the onset of

the single-step L–H (figure 8(b)), L–I–L (figure 10(c)) as well as the L–I–H transitions (figure 13(i)). This may indicate that the turbulence-driven $\mathbf{E} \times \mathbf{B}$ flow is in the electron diamagnetic drift direction inside the separatrix. Furthermore, the change in the $\mathbf{E} \times \mathbf{B}$ velocity appears to slightly lag behind the fluctuation suppression as indicated by the phase-space trajectory (figure 11), which is consistent with the picture of turbulence-driven flow, in which the turbulence suppression leads to the loss of driving force for the flows, and in turn, the flows decay in response to the turbulence suppression. In addition, during the I-phase the transient enhancement in the fluctuation level leads to an increase in the $\mathbf{E} \times \mathbf{B}$ velocity towards the electron diamagnetic drift direction (figure 13 (i)), which is consistent with the observations with the GPI diagnostic in EAST [40]. The velocity measured by the GPI diagnostic is the poloidal phase velocity of fluctuations in the laboratory frame, while the velocity measured by the probes is the $\mathbf{E} \times \mathbf{B}$ velocity. They are close to each other only in case when the fluctuation phase velocity in the plasma frame is much smaller than the $\mathbf{E} \times \mathbf{B}$ velocity.

- (5) One important distinction between the L–I–H and the L–I–L transitions has been observed, with respect to the time evolution of the edge pressure gradient and mean $\mathbf{E} \times \mathbf{B}$ flow during the I-phase. Both of them ramp up at the L–I–H transition, as measured directly by the probes inside the separatrix (figure 13), which is further evidenced by a gradual buildup of the radial gradient in the XUV radiations at the plasma edge, and a gradual increase in the central-line-averaged density and the plasma-stored energy (figure 15), suggesting that the global particle and energy confinements are improved. In contrast, there is no clear change during the L–I–L transitions (figures 15 and 9). This may indicate that a gradual buildup of the edge pressure gradient and mean $\mathbf{E} \times \mathbf{B}$ flow during the I-phase leads to the final transition into the H-mode, otherwise, the plasma may return to the L-mode. However, an open question still exists on this. Why the turbulence still recovers late in the I-phase when the mean flow shear has been significantly enhanced? In principle, a strong mean flow shear will stop the recovery if the turbulence drive does not increase accordingly.
- (6) As frequently seen during the L–I–H transition which ends up with an ELM-free phase, a gradual change from the LCOs to the type III ELMs appears. The former does not exhibit detectable precursor oscillations, while the latter is preceded by clear precursor activities (figures 13 and 17). However, the quiescent periods, τ_H , prior to the type III ELMs appear to be longer than those in the LCOs. The H–L back transition revisits the path at the forward transition with a gradual change from the type III ELMs, which show precursor oscillations, to the LCOs (figure 21). Meanwhile, the pedestal gradient is progressively reduced during the I-phase as evidenced by a gradual decrease in the radial gradient of the XUV radiations (figure 21(c)). In addition, the EAST experiments show that the I-phase can be observed both at the forward transition and at the back transition for both unfavourable and favourable ion ∇B directions, but much less frequently than those

with DN configuration, typically with much shorter I-phase duration. In contrast, the previous investigations on ASDEX Upgrade concluded that no LCO occurs for the unfavourable ion ∇B direction either at the forward transition or back transition [9].

- (7) Electron density, temperature, parallel flows in the co-current direction, $\mathbf{E} \times \mathbf{B}$ flows and diamagnetic flows in the ion diamagnetic direction are observed to be enhanced in the SOL during the transient enhancement of turbulent fluctuations in the I-phase. The parallel flow velocity measured by the Mach probe is strongly correlated with the Pfirsch–Schlüter (P–S) flow velocity at the outer midplane (figure 16). In general, the behaviours in the SOL appear to be a consequence of a periodic modulation in the turbulent fluctuations and cross-field transport at the plasma edge.
- (8) Significant magnetic perturbations, $|\delta B_p| \sim 1$ G, associated with the LCOs, have been detected by the Mirnov coils located on the chamber wall. The amplitude of the magnetic perturbations generally increases with decreasing oscillation frequencies. The magnetic perturbations exhibit $m/n = 1/0$ spatial structure, i.e., axisymmetric in the toroidal direction with nearly up–down anti-phase in the poloidal direction. The magnetic perturbations at the L–I–H, L–I–L and H–I–L transitions are similar in terms of the structure characteristics. The magnetic perturbations associated with the type III ELMs are typically stronger than those for the LCOs and exhibit similar spatial structures. However, they appear to have much stronger skewness relative to those for the LCOs, nearly in phase on the low-field side.
- (9) We do not see GAM in most cases near the transition threshold conditions on EAST. The GAMs were observed to decrease in amplitude or to be absent in DIII-D [29, 30] and HL-2A [31, 41, 59], as the transition is approached. However, GAMs were observed previously in ASDEX Upgrade during the I-phase and recently in C-Mod during the I-mode and the L-mode to I-mode transition using a newly implemented GPI diagnostics [69]. In C-Mod, the GAM was observed to interact with a weakly coherent mode, which seems to be the pumping wave of the GAMs.

Regarding the phase relationship between the $\mathbf{E} \times \mathbf{B}$ flow and the turbulence intensity during the I-phase, the type-Y LCO, i.e., the former slightly lags behind the latter, was observed at the L–I–L transition, which is consistent with the observation in the HL-2A tokamak [41, 59]. However, at the L–I–H transition, the poloidal $\mathbf{E} \times \mathbf{B}$ flow was observed to be enhanced in the electron diamagnetic drift direction almost at the same time of the transient enhancement in the turbulence intensity, as shown in figure 13(i). Similar flow change was also observed with the GPI diagnostic in EAST [40]. It should be pointed out that the phase in the $\mathbf{E} \times \mathbf{B}$ velocity measured by the Langmuir probe array strongly depends on how much T_e correction has been taken into account in the Φ_p and E_r calculation. The T_e has a significant contribution to the plasma potential, $\Phi_p = \Phi_f + \alpha T_e$, where α is taken as 2.5 throughout this paper. The two terms, Φ_f and αT_e , are usually comparable in magnitude at the plasma edge. The coefficient α is predicted to be 2.8 in unmagnetized deuterium plasmas according to the standard probe sheath theory [56]. However, in a strongly

magnetized plasma, α will be downshifted. There is currently no probe theory or empirical scaling in strongly magnetized plasmas to follow, so that there is still some uncertainty in the accuracy of the coefficient α . A very small T_e correction ($\alpha < 1$) could change the type-Y LCO to the type-J LCO. Nevertheless, a variation of α in the range of 2–2.8 will not qualitatively change the phase relationship reported in this paper. On the other hand, the probe data available for this analysis is still very limited due to the limited machine time and the accessibility of the probe diagnostic. Further experiments are required to accumulate more probe data in various divertor configurations. In addition, comparison with other edge flow and fluctuation diagnostics is required, such as Doppler back scattering and lithium beam probe, which will be available in the next experimental campaign on EAST.

Acknowledgments

This work was supported by National Magnetic Confinement Fusion Science Programme of China under Contracts Nos 2011GB107001, 2011GB101000, 2013GB106003, 2013GB107000, 2012GB101000, 2012GB112004 and 2010GB104001, National Natural Science Foundation of China under Contracts Nos. 11422546, 10990212, 10990210, 11321092, 11075181 and the Sino Danish Center for Education and Research.

References

- [1] Shimada M. et al 2007 Progress in the ITER Physics Basis: chapter 1. Overview and summary *Nucl. Fusion* **47** S1
- [2] Martin Y.R. et al 2008 *J. Phys.: Conf. Ser.* **123** 012033
- [3] Righi E. et al 1999 *Nucl. Fusion* **39** 309
- [4] Burrell K.H. et al 1990 *Phys. Fluids B* **2** 1405
- [5] Itoh S.-I., Itoh K., Fukuyama A. and Miura Y. 1991 *Phys. Rev. Lett.* **67** 2485
- [6] Zohm H. et al 1992 *Nucl. Fusion* **32** 489
- [7] Zohm H. et al 1994 *Phys. Rev. Lett.* **72** 222
- [8] Zohm H. et al 1994 *Plasma Phys. Control. Fusion* **36** A129
- [9] Zohm H. et al 1995 *Plasma Phys. Control. Fusion* **37** 437
- [10] Zohm H. 1996 *Plasma Phys. Control. Fusion* **38** 105
- [11] Cordey J. et al 1995 *Nucl. Fusion* **35** 505
- [12] Ido T. et al 2000 *Plasma Phys. Control. Fusion* **42** A309
- [13] Hirsch M. et al 1998 *Plasma Phys. Control. Fusion* **40** 631
- [14] Hirsch M. et al 2000 *Plasma Phys. Control. Fusion* **42** A231
- [15] Rudakov D.L. et al 2001 *Plasma Phys. Control. Fusion* **43** 559
- [16] Estrada T. et al 2010 *Europhys. Lett.* **92** 35001
- [17] Estrada T. et al 2011 *Phys. Rev. Lett.* **107** 245004
- [18] Estrada T. et al 2012 *Plasma Phys. Control. Fusion* **54** 124024
- [19] Colchin R.J. et al 2002 *Phys. Rev. Lett.* **88** 255002
- [20] Colchin R.J. et al 2002 *Nucl. Fusion* **42** 1134
- [21] Kim E.-J. and Diamond P.H. 2003 *Phys. Rev. Lett.* **90** 185006
- [22] Miki K. et al 2012 *Phys. Plasmas* **19** 092306
- [23] Miki K. et al 2013 *Nucl. Fusion* **53** 073044
- [24] Miki K. et al 2013 *Phys. Plasmas* **20** 062304
- [25] Miki K. et al 2013 *Phys. Rev. Lett.* **110** 195002
- [26] Miki K. et al 2013 *Phys. Plasmas* **20** 082304
- [27] Zweben S.J. et al 2010 *Phys. Plasmas* **17** 102502
- [28] Conway G.D. et al 2011 *Phys. Rev. Lett.* **106** 065001
- [29] McKee G.R. et al 2009 *Nucl. Fusion* **49** 115016
- [30] Yan Z. et al 2013 *Nucl. Fusion* **53** 113038
- [31] Xu M. et al 2012 *Phys. Rev. Lett.* **108** 245001
- [32] Xu G.S. et al 2011 *Phys. Rev. Lett.* **107** 125001
- [33] Schmitz L. et al 2012 *Phys. Rev. Lett.* **108** 155002
- [34] Sechrest Y. et al 2011 *Phys. Plasmas* **18** 012502
- [35] Zweben S.J. et al 2012 *Plasma Phys. Control. Fusion* **54** 025008
- [36] Manz P. et al 2012 *Phys. Plasmas* **19** 072311
- [37] Xu G.S. et al 2012 *Phys. Plasmas* **19** 122502
- [38] Wang H.Q. et al 2012 *Nucl. Fusion* **52** 123011
- [39] Tynan G.R. et al 2013 *Nucl. Fusion* **53** 073053
- [40] Xu G.S. et al 2014 *Nucl. Fusion* **54** 013007
- [41] Cheng J. et al 2013 *Phys. Rev. Lett.* **110** 265002
- [42] Kobayashi T. et al 2013 *Phys. Rev. Lett.* **111** 035002
- [43] Hill D.N. and the DIII-D Team 2013 *Nucl. Fusion* **53** 104001
- [44] Guo Z.B. and Diamond P.H. et al 2013 private communication
- [45] Xu G.S. 2013 *AAPPS Bull.* **23** 9 <http://aappsbulletin.org>
- [46] Zhang W. et al 2010 *Rev. Sci. Instrum.* **81** 113501
- [47] Xu G.S. et al 2011 *Nucl. Fusion* **51** 072001
- [48] Zhang X.J. et al 2013 *Nucl. Fusion* **53** 023004
- [49] Wan B.N. et al 2013 *Nucl. Fusion* **53** 104006
- [50] Guo H.Y. et al 2014 *Nucl. Fusion* **54** 013002
- [51] Wan B.N. et al 2009 *Nucl. Fusion* **49** 104011
- [52] Schrittwieser R. et al 2013 *40th EPS Conf. on Plasma Physics (Espoo, Finland, 1–5 July 2013)* P6.017, <http://ocs.ciemat.es/EPS2013PAP/pdf/P6.017.pdf>
- [53] Xu G.S. et al 2003 *Phys. Rev. Lett.* **91** 125001
- [54] Liu A.D. et al 2009 *Phys. Rev. Lett.* **103** 095002
- [55] Zhao K.J. et al 2006 *Phys. Rev. Lett.* **96** 255004
- [56] Hutchinson I.H. 2002 *Principles of Plasma Diagnostics* (Cambridge: Cambridge University Press)
- [57] Xu G.S. et al 2011 *Plasma Sci. Technol.* **13** 397
- [58] Yan Z. et al 2014 *Phys. Rev. Lett.* **112** 125002
- [59] Zhao K.J. et al 2013 *Nucl. Fusion* **53** 123015
- [60] McKee G.R. et al 2004 *Rev. Sci. Instrum.* **75** 3490
- [61] Holland C. et al 2004 *Rev. Sci. Instrum.* **75** 4278
- [62] Zhang T. et al 2013 *Phys. Lett. A* **377** 1725
- [63] Novakovskii S.V. et al 1997 *Phys. Plasmas* **4** 4272
- [64] D'Ippolito D.A. et al 2011 *Phys. Plasmas* **18** 060501
- [65] Xiong H. et al 2013 *Radiat. Effects Defects Solids* **168** 873
- [66] Müller S. 2013 Turbulence and flow measurements in the X-point region during L–I–H transition in ASDEX Upgrade *H-Mode Workshop (Fukuoka, Japan, 2–4 October 2013)* P01-17, <http://tokusui.riam.kyushu-u.ac.jp/HmodeWS2013/>
- [67] Ma Y. et al 2012 *Nucl. Fusion* **52** 023010
- [68] Shaing K.C. et al 1995 *Phys. Plasmas* **2** 1801
- [69] Cziegler I. et al 2013 *Phys. Plasmas* **20** 055904